UC Berkeley
UC Berkeley Previously Published Works

Title

Anticipating how rain-on-snow events will change through the 21st century: lessons from the 1997 new year's flood event

Permalink

https://escholarship.org/uc/item/5q01j5w7

Journal

Climate Dynamics, 62(9)

ISSN

0930-7575

Authors

Rhoades, Alan M

Zarzycki, Colin M

Hatchett, Benjamin J

et al.

Publication Date

2024-09-01

DOI

10.1007/s00382-024-07351-7

Peer reviewed

ORIGINAL ARTICLE

Anticipating how rain-on-snow events will change through the 21st century: lessons from the 1997 new year's flood event

Alan M. Rhoades[1] · Colin M. Zarzycki[2] · Benjamin J. Hatchett[3] · Héctor Inda-Diaz[1] · William Rudisill[1] ·
Benjamin Bass[4] · Eli Dennis[4] · Anne Heggli[5] · Rachel McCrary[6] · Seth McGinnis[6] · Mohammed Ombadi[7] ·
Stefan Rahimi-Esfarjani[8] · Emily Slinskey[9] · Abhishekh Srivastava[10] · Julia Szinai[1] · Paul A. Ullrich[1,10,11] ·
Michael Wehner[12] · David Yates[6] · Andrew D. Jones[1,13]

Abstract

The California-Nevada 1997 New Year's flood was an atmospheric river (AR)-driven rain-on-snow (RoS) event and remains the costliest in their history. The joint occurrence of saturated soils, rainfall, and snowmelt generated inundation throughout northern California-Nevada. Although AR RoS events are projected to occur more frequently with climate change, the warming sensitivity of their flood drivers across scales remains understudied. We leverage the regionally refined mesh capabilities of the Energy Exascale Earth System Model (RRM-E3SM) to recreate the 1997 New Year's flood with horizontal grid spacings of 3.5 km across California, with forecast lead times of up to 4 days, and across six warming levels ranging from pre-industrial conditions to +3.5 °C. We describe the sensitivity of the flood drivers to warming including AR duration and intensity, precipitation phase, intensity and efficiency, snowpack mass and energy changes, and runoff efficiency. Our findings indicate current levels of climate change negligibly influence the flood drivers. At warming levels ≥ 1.7 °C, AR hazard potential increases, snowpack nonlinearly decreases, antecedent soil moisture decreases (except where the snowline retreats), and runoff decreases (except in the southern Sierra Nevada where antecedent snowpack persists). Storm total precipitation increases, but at rates below warming-induced increases in saturation-specific humidity. Warming intensifies short-duration, high-intensity rainfall, particularly where snowfall-to-rainfall transitions occur. This study highlights the nonlinear tradeoffs in 21st-century RoS flood hazards with warming and provides water management and infrastructure investment adaptation considerations.

✉ Alan M. Rhoades
arhoades@lbl.gov

1 Earth and Environmental Sciences Area, Lawrence Berkeley National Laboratory, Berkeley, CA, USA

2 Department of Meteorology and Atmospheric Science State, Penn State University, State College, PA, USA

3 Cooperative Institute for Research in the Atmosphere, Colorado State University, Fort Collins, CO, USA

4 Institute of the Environment and Sustainability, University of California, Los Angeles, Los Angeles, CA, USA

5 Division of Atmospheric Sciences, Desert Research Institute, Reno, NV, USA

6 Research Applications Lab, National Center for Atmospheric Research, Boulder, CO, USA

7 Department of Climate and Space Sciences and Engineering, University of Michigan, Ann Arbor, MI, USA

8 Department of Atmospheric Science, University of Wyoming, Laramie, WY, USA

9 Center for Western Weather and Water Extremes, Scripps Institution of Oceanography, San Diego, CA, USA

10 Department of Land, Air, and Water Resources, University of California, Davis, Davis, CA, USA

11 Physical and Life Sciences Directorate, Lawrence Livermore National Laboratory, Livermore, CA, USA

12 Applied Mathematics and Computational Research Division, Lawrence Berkeley National Laboratory, Berkeley, CA, USA

13 Energy and Resources Group, University of California, Berkeley, Berkeley, CA, USA

1 Introduction

Climate change acts on temperature patterns and their magnitudes (Santer et al. 2013; Bindoff et al. 2013; Eyring et al. 2021) to amplify, diminish, and/or shift the timing of the fluxes and stores of the hydrologic cycle (Pepin et al. 2015; Allan et al. 2020). These dynamical and thermodynamical feedbacks influence the large-scale transport of water vapor via atmospheric rivers (ARs) (Payne et al. 2020), their local-scale storm characteristics (Rhoades et al. 2020b), and the land surface response through their alterations to snowpack lifecycles (Siirila-Woodburn et al. 2021) and soil moisture feedbacks (Lehner and Coats 2021). As a result, a detectable climate change-induced alteration to the intensity and frequency of inter-annual hydroclimate variability (e.g., multi-year droughts and occasional pluvials) and intra-annual hydrometeorological extremes (e.g., compound flood events) is currently underway in the western United States, particularly in mountains (Stevenson et al. 2022). For communities residing within and downstream of western United States mountains, the dynamical and thermodynamical fingerprints of climate change have already started to shape both headwater hydrology and downstream flood hazards (Hock et al. 2019; Immerzeel et al. 2020; Rhoades et al. 2022).

Rainfall-induced flood hazards in the western United States maritime mountains are projected to amplify by more than seven times in a warmer world (Ombadi et al. 2023). This projected amplification of flood hazards has been, in part, tied to increases in the frequency of moderate to extreme ARs and back-to-back AR events (Huang et al. 2020; Rhoades et al. 2021; Corringham et al. 2022; Bowers et al. 2023). AR-related precipitation increases (or scales) at larger rates with warming than non-AR events across both daily average and maximum hourly timescales in gridded observational products (Najibi and Steinschneider 2023) and models (Rhoades et al. 2020b). Theory has been developed for how warming will alter AR-mountain interactions, from both a thermodynamical (e.g., microphysics) and dynamical (e.g., orographic uplift) perspective (Siler and Roe 2014). Thermodynamically-induced changes arise through alterations in the lifting condensation level, in cloud collision-coalescence processes, and hydrometeor fall speeds (i.e., raindrops fall at a 5–10× faster rate than snowflakes; Rhoades et al. 2018). Dynamical responses to warming also influence microphysical processes, particularly in maritime mountains that are typically orthogonal to landfalling ARs. The net result is an alteration to the character of AR-derived mountain precipitation (e.g., intensity, duration, and phase), precipitation efficiency (i.e., the amount of atmospheric water vapor extracted as precipitation), and windward versus leeward precipitation ratios.

Although theory supports that AR-mountain precipitation could be enhanced through the Clausius–Clapeyron relationship, theory also suggests a warmer world will increase static stability in mountains, inhibiting orographic uplift and limiting precipitation scaling with warming (Siler and Roe 2014). However, evidence for a warming-induced decrease in precipitation with elevation in the observational record is weak (Pepin et al. 2022). This may be attributed to a lack of consistent, high-density measurements in mountains. Nonetheless, reanalysis and observationally-based gridded products clearly show warming-induced reductions in precipitation with elevation, particularly in midlatitudes (Pepin et al. 2022). Reanalysis products and future climate model projections have also shown that warming can weaken steering winds (e.g., zonal winds at 700 mb) that guide storms, resulting in reduced orographic precipitation (Luce et al. 2013). Finally, Patricola et al. (2022) found ARs that are weakly linked with an extra-tropical cyclone can have decreased precipitation scaling with warming and have an increased precipitation scaling with strong extra-tropical cyclones.

The flood hazards associated with a transition from snow to rain in a warmer world could be enhanced during compound extreme events (AghaKouchak et al. 2020; Ombadi et al. 2023). Compound extreme events can amplify flood hazards, especially to vulnerable communities, infrastructure, and ecosystems due to a combination of hydrometeorological drivers that overlap in space and/or time (Zscheischler et al. 2018). Rain-on-snow (RoS) events are one such type of compound extreme events (McCabe et al. 2007) that enhances flood risk, especially if the snowpack is actively contributing meltwater (Brandt et al. 2022) or if antecedent soils are saturated (Haleakala et al. 2022). Such situations often occur in maritime mountains such as the Sierra Nevada in the western United States (Guan et al. 2016). For example, 50% of RoS events in the Sierra Nevada are associated with ARs, and AR-induced RoS events have 50% higher streamflow/precipitation ratios than non-RoS AR events (Guan et al. 2016). RoS events include 50–80% higher peak flows than typically occur under spring snowmelt in the central Sierra Nevada (Kattlemann 1997). In a warmer world, the Sierra Nevada is projected to see an increase in RoS event frequency at higher elevations and, under the right circumstances, runoff volumes could increase by more than 200% (Musselman et al. 2018). However, due to the spatiotemporal heterogeneity and nonlinear interactions between the fluxes and stores of water during a RoS event, flood hazard to downstream communities may increase up to a certain warming level (e.g., López-Moreno et al. (2021) found that snowmelt during RoS events increases by 8–27% per +1 °C) and then decrease once low-to-no snow conditions emerge (Rhoades et al. 2022). The decrease in flood hazard

potential presented by RoS events in a low-to-no snow future does not mean that flood hazards will completely go away as rainfall-dominated floods activate a larger contributing area and can exceed RoS event flood potential (Davenport et al. 2020).

The New Year's flood event of 1997, hereafter referred to as the 1997 flood, is an object lesson (or case study) of a RoS event that had substantial societal implications in both California and Nevada (Tarouilly et al. 2021). The 1997 flood featured land surface preconditioning (e.g., saturated soils and accumulation of an above normal snowpack, even at lower elevations, following an extremely wet November-December) and a strong landfalling AR event that elevated freezing levels to nearly 3000 m, and resulted in widespread snowmelt following prolonged rainfall (Rhoades et al. 2023). California and Nevada recorded widespread flooding in 18 river basins and approached or exceeded all-time records on six of them (e.g., Carson, Cosumnes, Napa, South Fork American, Truckee, and Walker rivers) (Lott et al. 1997). The combination of spatiotemporally compounding hydrometeorological drivers inundated low-lying urban and agricultural areas throughout California with more than 1.5 billion US dollars in estimated damages (Lott et al. 1997). Flooding occurred in higher elevations as well, with the Yosemite Valley experiencing floodwaters 2 m deep (Jackson et al. 1997).

To explore how the flood drivers of the 1997 flood could respond to warming, we designed numerical experiments following a storyline framework (Shepherd et al. 2018; Shepherd 2019). Storylines are one approach to explore stress tests on water management and proactively identify climate adaptation strategies (Albano et al. 2021). In Rhoades et al. (2023), we simulated the 1997 flood "event that was" as realistically as possible. This study identified that the regionally refined mesh capabilities of the Energy Exascale Earth System Model (RRM-E3SM) with the appropriate horizontal resolution and forecast lead time is fit-for-purpose to recreate several of the major hydrometeorological drivers of the 1997 flood. This historical skill in capturing the various land-atmosphere interactions provides confidence that the model could be used to investigate the sensitivity of the physical drivers of the 1997 flood to climate change and how they interact to offset or enhance flood potential. Here, we construct simulations of the "event that might be" in both past and future climates. Storylines of this nature have been used in both event attribution (e.g., Pall et al. 2017) and future projection contexts (e.g., Patricola et al. 2022). This approach is analogous to the pseudo-global warming approach oft employed by regional climate models (Schär et al. 1996; Ullrich et al. 2018; Gutowski et al. 2020; Brogli et al. 2023), yet is produced using an Earth system model. We aim to answer several scientific questions framed around the 1997 flood drivers including:

(1) How might AR characteristics (i.e., integrated water vapor and transport) differ with warming levels?
(2) How might warming levels alter storm characteristics across durations from minutes to several days?
(3) How sensitive might the antecedent snowpack and the net snowmelt over the storm duration be to warming levels?
(4) How might mountain runoff, particularly runoff contributed by snowmelt, respond to warming?

Addressing these questions will provide the scientific community and water managers with information to prepare for potential climate change impacts on AR precipitation characteristics and the resulting flood response driven by soil moisture, snowmelt, and runoff conditions. This study represents a pioneering effort in utilizing an Earth system model to simulate and forecast the atmosphere-through-bedrock response of a compound extreme event across historical, contemporary, and future climate scenarios. Further, the 1997 flood event is both understudied and underutilized in detection and attribution studies of climate change, despite its recognized importance as a design storm in water management. We begin by introducing the experimental setup to recreate the 1997 flood at various warming levels. To address our research questions, we discuss how the hydrometeorological characteristics of the 1997 flood changed across warming levels. We find that warming level enhances an AR's propensity to produce hazards, particularly due to an enhancement of precipitation at hourly-to-subhourly timescales. Antecedent snowpacks and storm duration snowmelt ubiquitously decline with warming. Statewide runoff responses at both storm duration and subdaily timeframes are muted with warming but have important dependencies in the northern versus southern Sierra Nevada during different moments of the flood. These spatiotemporal dependencies highlight how warming could shift RoS hazard potential to the southern Sierra Nevada, which has important implications for regional and statewide water and natural hazard management and adaptation planning.

2 Methods

To simulate the 1997 flood, we employ the U.S. Department of Energy-funded Energy Exascale Earth System Model (E3SM) version 2 (Golaz et al. 2022; Tang et al. 2022; Harrop et al. 2023). To ensure that the 1997 flood event hydrometeorological characteristics are skillfully recreated, we leverage the regionally refined mesh capabilities of E3SM (RRM-E3SM) at 3.5 km grid spacing centered over California that progressively coarsens to 111 km grid spacing globally (Rhoades et al. 2023). The E3SMv2 dynamical core is described in Taylor et al. (2020) and Golaz et al. (2022).

Atmospheric radiation is handled by the Rapid Radiative Transfer Model (Mlawer et al. 1997). Other subgrid-scale physics schemes include those that account for aerosols (Wang et al. 2020), deep convection (Zhang and McFarlane 1995), gravity waves (Richter et al. 2010), microphysics (Gettelman and Morrison 2015), macrophysics, shallow convection, and turbulence (Larson 2022), with some recent modifications outlined in Golaz et al. (2022). The RRM-E3SM simulations use Atmosphere Model Intercomparison Project (AMIP) protocols (Gates et al. 1999) whereby the atmospheric (E3SM Atmosphere Model; EAM) and land surface (E3SM Land Model; ELM) sub-component models of E3SM are two-way coupled and lower boundary sea surface temperatures and sea ice conditions are prescribed. A detailed explanation of the RRM-E3SM (3.5 km) model experimental setups is provided in Rhoades et al. (2023).

The spatiotemporal warming level signatures for each climate initial condition are derived by extracting the 40-member ensemble mean Community Earth System Model version 1 Large Ensemble (CESM LENS) monthly temperature, specific humidity, and sea surface temperature fields at the desired global warming level over the simulation period of 1920–2100 (Kay et al. 2015). Pre-industrial simulations are derived using CESM LENS atmospheric and oceanic fields from 1921. We acknowledge a small amount of warming occurred between 1850 and 1920 (approximately +0.1 °C; see fig. 2 of Kay et al. 2015), however, we opt to use the pre-industrial naming convention to maintain consistency with Pettett and Zarzycki (2023). We simulate the 1997 flood under the observed atmospheric, land and oceanic conditions in 1997, called the "control" simulation (Rhoades et al. 2023). Then, we simulate the 1997 flood event under "contemporary" atmospheric and oceanic conditions where the CESM-LENS ensemble average reaches a global-mean value of +1°C of warming (in 2019) relative to 1920 in the atmosphere over both the ocean and land. The other three sustained warming level simulations are derived from the year in which the CESM-LENS ensemble mean global-mean temperature difference (from 1920) reaches +2 °C (in 2044), +3 °C (in 2063), and +4 °C (in 2081). The two-dimensional sea surface temperature and three-dimensional changes in specific humidity and air temperature are then applied from the CESM-LENS ensemble mean monthly climatology using that specific year and the month that the storyline event occurred (e.g., January 2081). Therefore, the actual global warming levels of reference height temperature (2 m) over global land relative to the control simulation of the 1997 flood, are +0.1°C (pre-industrial), +0.4°C (contemporary), +1.7°C, +2.5°C, and +3.5°C. Notably, the pre-industrial simulation has a slightly warmer global temperature delta than the control simulation (Fig. S1). This is due to the phenomenon known as the Early Twentieth Century Warming (1890s to 1940s) that featured relatively

high Arctic warming between the 1920s and 1930s (Hegerl et al. 2018) (as confirmed in Fig. S1).

To derive initial and boundary conditions for the EAM forecasts, we leverage the Betacast software suite first described in Zarzycki and Jablonowski (2015) and available on GitHub - https://github.com/zarzycki/betacast. Initial atmospheric conditions are generated by remapping the fifth generation of the European Centre for Medium-Range Weather Forecasts (ECMWF) reanalysis, ERA5 (Copernicus Climate Change Service Climate Data Store (CDS) 2017). State fields are adjusted following Trenberth (1995) to account for geostrophic (e.g., surface pressure) imbalances arising from differences between ERA5 and RRM-E3SM topography representations. The ERA5 atmospheric temperature and specific humidity fields are spatiotemporally adjusted with the mean CESM LENS deltas at the warming levels mentioned previously. The specific process is outlined in further detail in Appendix A of Pettett and Zarzycki (2023). Ocean and ice forcing are generated by interpolating the NOAA Optimum Interpolation ocean surface conditions (Reynolds et al. 2007). For the perturbed simulations, a monthly time series of warming deltas for the aforementioned variables are generated by averaging the CESM LENS across ensemble members and subtracting the monthly mean in 1920 from each of the corresponding months between 1921 and 2100. These deltas are horizontally and vertically interpolated and added to the atmospheric initial conditions and applied to the ocean and ice boundary conditions. In cases where the warming level results in the surface temperature going above freezing the corresponding ice grid cell is converted to ocean. Ocean-to-ice grid cell conversions occur when the surface temperature is below freezing.

The ELM initial land surface conditions are provided by reforecasting five years before the EAM forecasts at three-hourly timesteps with ERA5 atmospheric boundary conditions. This mimics a data assimilation process where the land model is continually forced by the observed state of the atmosphere leading up to the coupled model initialization. This standalone simulation allows for the land-surface antecedent conditions (e.g., soil moisture concentrations and snowpack) to equilibrate under the desired warming level. For example, the snowpack depths and extents and soil moisture concentrations adjust to the new specific humidity and temperatures at each warming level over the five years. A five-year spin-up of the land-surface conditions before the 1997 flood is deemed to be a credible assumption for California as it is dominated by seasonal and ephemeral rather than perennial snowpacks (Hatchett et al. 2023) and root zone soil moisture memory is, generally, 2 to 4 months (Kumar et al. 2020).

For each warming level, we produce six initial condition forecasts with lead times of up to 4 days before 01 January

1997. Each forecast represents a plausible representation of the land-surface antecedent conditions before the 1997 flood as well as the landfalling progression of the AR. Forecasts were initialized 12 h apart (i.e., 28 December 1996 at 00Z up to 30 December 1996 at 12Z) and each successive forecast leverages the previous forecast as an initial condition. Rhoades et al. (2023) showed that the RRM-E3SM (3.5 km) simulation flood drivers (e.g., AR characteristics, storm total precipitation, and change in snow water equivalent) were relatively insensitive to forecast lead times of 2–4 days when recreating the 1997 flood event. Therefore, we use six forecast averages of the RRM-E3SM (3.5 km) grid for our warming level comparisons.

In the RRM-E3SM (3.5 km) forecasts, we track ARs in the 1997 flood event using TempestExtremes (Ullrich and Zarzycki 2017; Ullrich et al. 2021) and their landfalling characteristics (e.g., AR category scales) using extensions made to TempestExtremes (Rhoades et al. 2020a, b, 2021). TempestExtremes AR detection is customizable and relies on both IVT and latitudinal thresholds and geometric parameters to isolate ARs from the background IVT. It is representative of a median-performing algorithm across different AR characteristics (e.g., number of AR events over a climatological period) in the Atmospheric River Tracking Method Intercomparison Project (Shields et al. 2018). In a future climate context, TempestExtremes highlighted an increase in the number of ARs with warming across the globe (again, representative of the median AR detector), yet the AR's area did not appreciably change with warming compared with other AR detectors (O'Brien et al. 2022). This is likely due to its use of both absolute thresholds for IVT as well as geometric constraints. Notably, since the 1997 flood was AR-generated, we leave the subgrid-scale parameterization deep convection scheme on across RRM-E3SM (3.5 km) simulations. This choice had a minimal influence on storm total precipitation, particularly in complex terrain, where nearly every grid cell was dominated by stratiform precipitation (as shown in Fig. S2).

For a quantitative albeit first-order evaluation of minimum snowmelt during the 1997 flood, we calculated two diagnostic snowpack variables critical to understanding RoS events: storm total advected energy and the change in cold content over the storm duration. Storm total represents the cumulative total of a given variable (e.g., snowmelt or rainfall) between the start of the 1997 flood (31 December 1996) up to the end (04 January 1997). Advected energy is the direct transfer of energy from rainfall into the snowpack. We use Equation 6.24 in DeWalle and Rango (2008) to compute advected energy (A; MJ/m^2):

$$A = c_w * \rho_w * P * (T_r - T_s)$$

where c_w is the specific heat of liquid water (4.184 J/kg/K), ρ_w is the density of liquid water (997. kg/m^3), P is the precipitation rate (m/s), T_r is the temperature of the rain (K), and T_s is the average snow temperature (K). We then convert advected energy from units of J/m^2/hour to units of MJ/m^2 via the relationship that 1 Watt-hour equals 0.0036 MJ at 6-hourly frequency. The advected energy equation is a function of precipitation intensity and the difference between the temperature of the precipitation and the temperature of the snowpack. Here, the temperature of the snowpack is derived from ELM, and we assume that the two-meter surface air temperature is representative of the precipitation temperature (as is done in Equation 6.24). Notably, advected energy is often quite small (less than 20% of total energy) compared to the sensible and latent heat fluxes that arise during a RoS event. This is important to note as RoS events not only produce higher runoff efficiencies due to the transfer of energy from the raindrops into a snowpack but also are driven by the formation of preferential flow paths with direct terrestrial water input (Heggli et al. 2022; Brandt et al. 2022).

Cold content is the vertically integrated internal energy of the snowpack and helps indicate whether the snowpack can begin to melt. We use Equation 6.27 in DeWalle and Rango (2008) to compute cold content (Q_{cc}; MJ/m^2):

$$Q_{cc} = c_i * \rho_s * h_s * (T_s - T_m)$$

where c_i is the specific heat of ice (0.00209 MJ/kg*K), ρ_s is the density of the snowpack (kg/m^3), h_s is the snow depth (m), T_s is the average snow temperature (K), and T_m is the melting temperature of ice (273.15 K). The calculation of cold content factors in the snowpack depth, density, and temperature. Once cold content reaches zero, additional energy introduced into the snowpack produces snowmelt. Cold content change was calculated between the start and end of the 1997 flood.

Snow hydrology representation in ELM is largely inherited from the Community Land Model version 5 (CLM5) of the Community Earth System Model (Danabasoglu et al. 2020; Golaz et al. 2022). ELM has up to a 12-layer snow model and the average temperature across these layers is used when computing both advected energy and the cold content. To estimate snowmelt, ELM first determines the surface fluxes and snow/soil temperatures (see Lawrence et al. (2019) and Section 2.8 of the CLM5 Technical Note - https://escomp.github.io/ctsm-docs/versions/master/html/tech_note/Snow_Hydrology/CLM50_Tech_Note_Snow_Hydrology.html). During isothermal conditions at 0°C in the snowpack (i.e., zero cold content), water transfer is estimated in the top snow layer. When the liquid generated in that layer exceeds a determined water holding capacity it is added to the underlying layer. The effective porosity (determined by ice content) of the underlying layer can either allow or

inhibit the transfer of water. This is repeated from the top snowpack layer down to the bottom snowpack layer. Notably, ELM (and many other land surface models) do not represent some of the internal snowpack physics that occur during RoS or melt events that recent observational and modeling studies increasingly highlight the importance of (Brandt et al. 2022; Heggli et al. 2022; Haleakala et al. 2022; Katz et al. 2023). For example, preferential flow paths (or "flow fingers") within the snowpack rather than a uniform wetting front can influence the snowmelt dynamics (McGurk and Marsh 1995; Brandt et al. 2022).

3 Results

We now investigate how warming alters the cross-scale interactions that shaped the hazard potentials of the 1997 flood event. We first investigate how warming alters the steering and moisture transport of the AR that occurred during the 1997 flood at planetary-to-synoptic scales. We then focus on synoptic-to-regional scales and investigate how AR characteristics, regional circulation drivers of precipitation, and storm event characteristics change with warming. Last, we end at regional-to-local scales and identify how warming modifies RoS characteristics of the 1997 flood through alterations to the antecedent and storm duration changes in snowpack, soil moisture, and runoff.

3.1 Atmospheric dynamics at synoptic-to-mesoscales are weakly influenced by warming, yet the hazard potential of the atmospheric river increases

Planetary-to-synoptic scale spatiotemporal snapshots of the integrated vapor transport (IVT) and geopotential height fields during the four days of the 1997 flood across different warming levels indicate different responses (Fig. S3). Notably, changes in the warming levels enhance IVT but result in a negligible effect on the 850 mb geopotential height fields. The different influences of warming on the IVT and geopotential height fields is preserved at regional-to-local scales near the California-Oregon coastline, too (Fig. 1). Changes in synoptic scale geopotential height fields are likely minimal due to how we performed the storyline simulation, which is more focused on how climate change influences thermodynamical rather than dynamical feedbacks. For example, as our simulations do not perturb the large-scale wind fields at initialization, we will not capture large-scale shifts in AR storm tracks due to spatiotemporal variations in the jet stream (although more local dynamical adjustment in the wind fields should occur).

This weak relationship between warming level and dynamical response is exhibited at more local scales in one

of the most important dynamical drivers of regional and orographic precipitation patterns in California: the Sierra Barrier Jet (SBJ). The SBJ occurs along the windward side of the Sierra Nevada and arises due to the blocking, slowing, and turning of low-level winds which, in turn, generates a southerly jet core that arises between 950–900 hPa with wind speeds of 15–30 m/s (Neiman et al. 2010; Hughes et al. 2012; Neiman et al. 2013). By influencing moisture advection and ascent at the regional scale, the SBJ is largely responsible for why the climatological precipitation maxima in California is located northwest of the Sierra Nevada and not consistently along the windward side of the Sierra Nevada where the orographic ascent of storms is maximized. The insensitivity of the horizontal and vertical structure of the SBJ to warming across all days of the 1997 flood are shown in Figs. S4, S6, S8, S10, and S12). Figs. S5, S7, S9, and S11 show the differences between the control and warming level experiments from the horizontal perspective of the SBJ (depicted at the intersection of the dotted lines in each figure) across all days of the 1997 flood.

Consistent with expectations from the Clausius–Clapeyron relationship, Fig. 2 indicates an intensification of landfalling AR characteristics of the 1997 flood across warming levels for 31 December 1996 up to 4 January 1997. One metric to assess AR hazard is the AR category (Ralph et al. 2019), which accounts for both the maximum intensity and duration of the AR. The region over which the landfalling AR reaches category 4 or 5 conditions, "mostly to primarily hazardous to water resource management", substantially expands in areal extent, spanning the entirety of northern-central California at the highest warming level (Fig. 2 and Fig. S13). This is primarily driven by monotonic increases in the maximum integrated water vapor reached during the 1997 flood at warming levels ≥ 1.7 °C combined with systematically stronger total winds in northern California (Fig. 2). The largest increases in maximum integrated water vapor occur in the central to southern coasts of California, however, winds over southern California are systematically reduced with warming. This offsetting interplay between thermodynamical and local dynamical drivers of AR character in the lower midlatitudes of the coastal western United States with warming was shown by Payne et al. (2020). We also show in Fig. 1 that a slight northward shift in the local dynamical fields (i.e., 850mb geopotential height contours) in response to warming could have influenced the weakened local winds in southern California.

3.2 Warming leads to more rainfall, via an enhancement in short duration, extreme rainfall

How the characteristics of the AR changes with warming is important to understand. This is because subcomponents

Fig. 1 **a** RRM-E3SM (3.5 km) forecast average estimate of the control simulation integrated vapor transport (IVT) on 01 January 1997. Difference plots (left column) represent differences between the control simulation and the pre-industrial (**a**), contemporary (**b**), +1.7 °C (**c**), +2.5 °C (**d**) and +3.5 °C (**e**) experiments. The center (right) column shows the 850mb geopotential heights (lines; units in meters) over California (Northeast Pacific) with the control simulation estimate (gray-to-white contours) underlying each warming level estimate (colored lines)
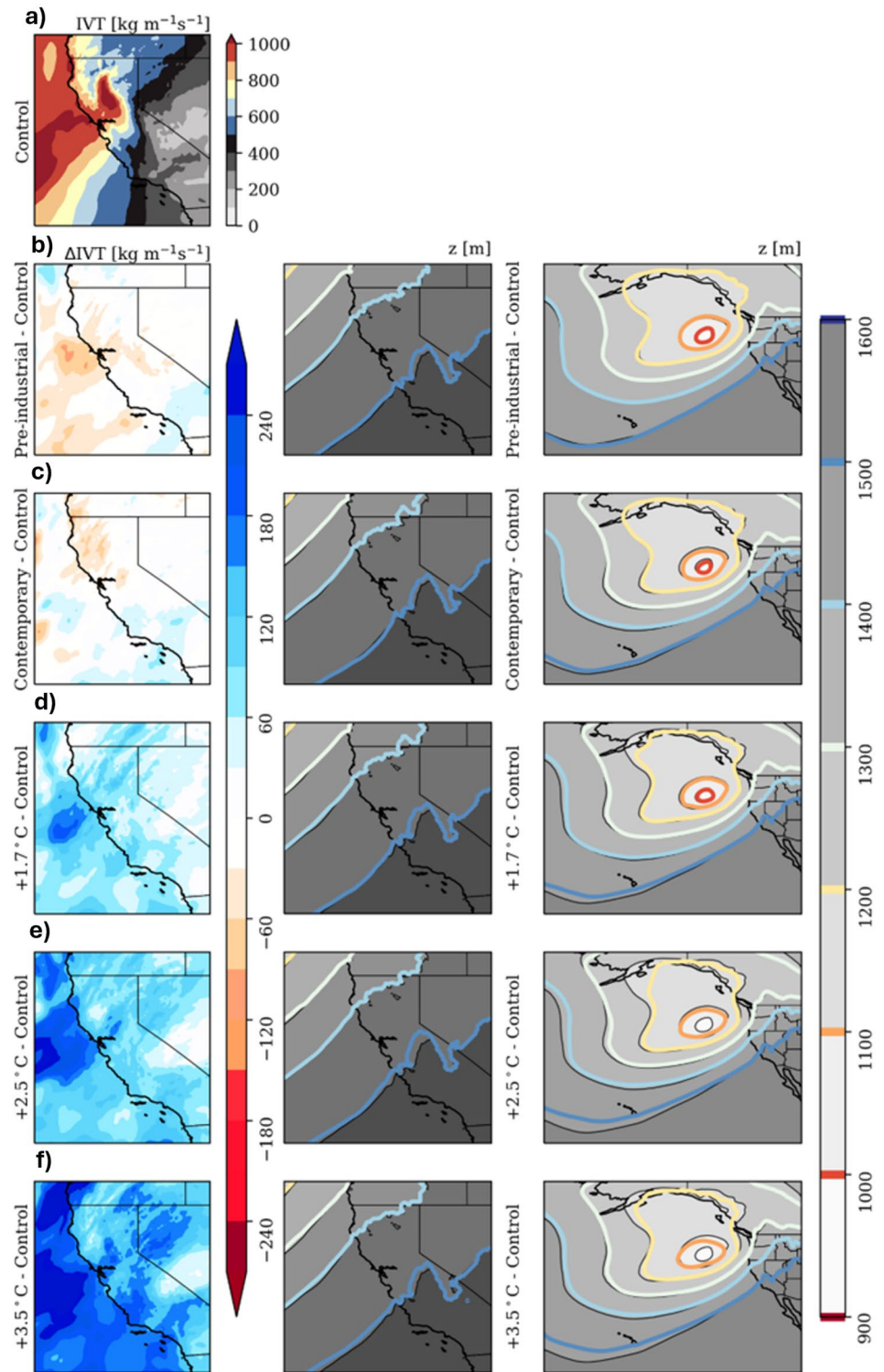
of an AR, such as integrated water vapor and winds, only represent the potential for precipitation to occur. That potential for precipitation depends on the topography, the orthogonality of moisture flux to the topography, the vertical velocity, the atmospheric stability, and cloud microphysical processes (Siler and Roe 2014; Rhoades et al. 2018; Ricciotti and Cordeira 2022). Figure S14 shows how different aspects of the precipitation characteristics of the 1997 flood were simulated and their warming level sensitivities. Changes in storm total precipitation with warming levels have different spatial signatures in the northern versus southern portions of California (Fig. 3). Given that
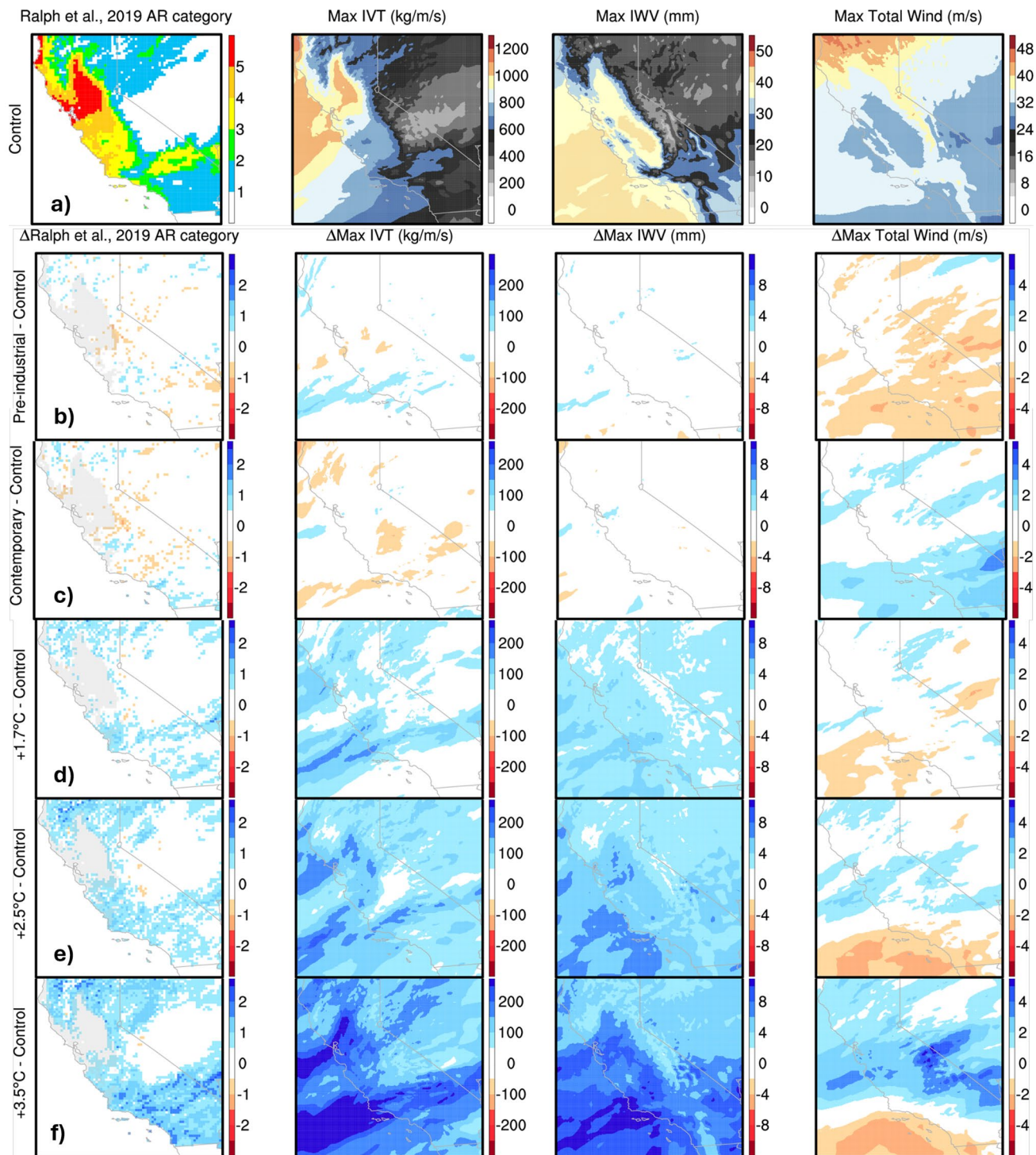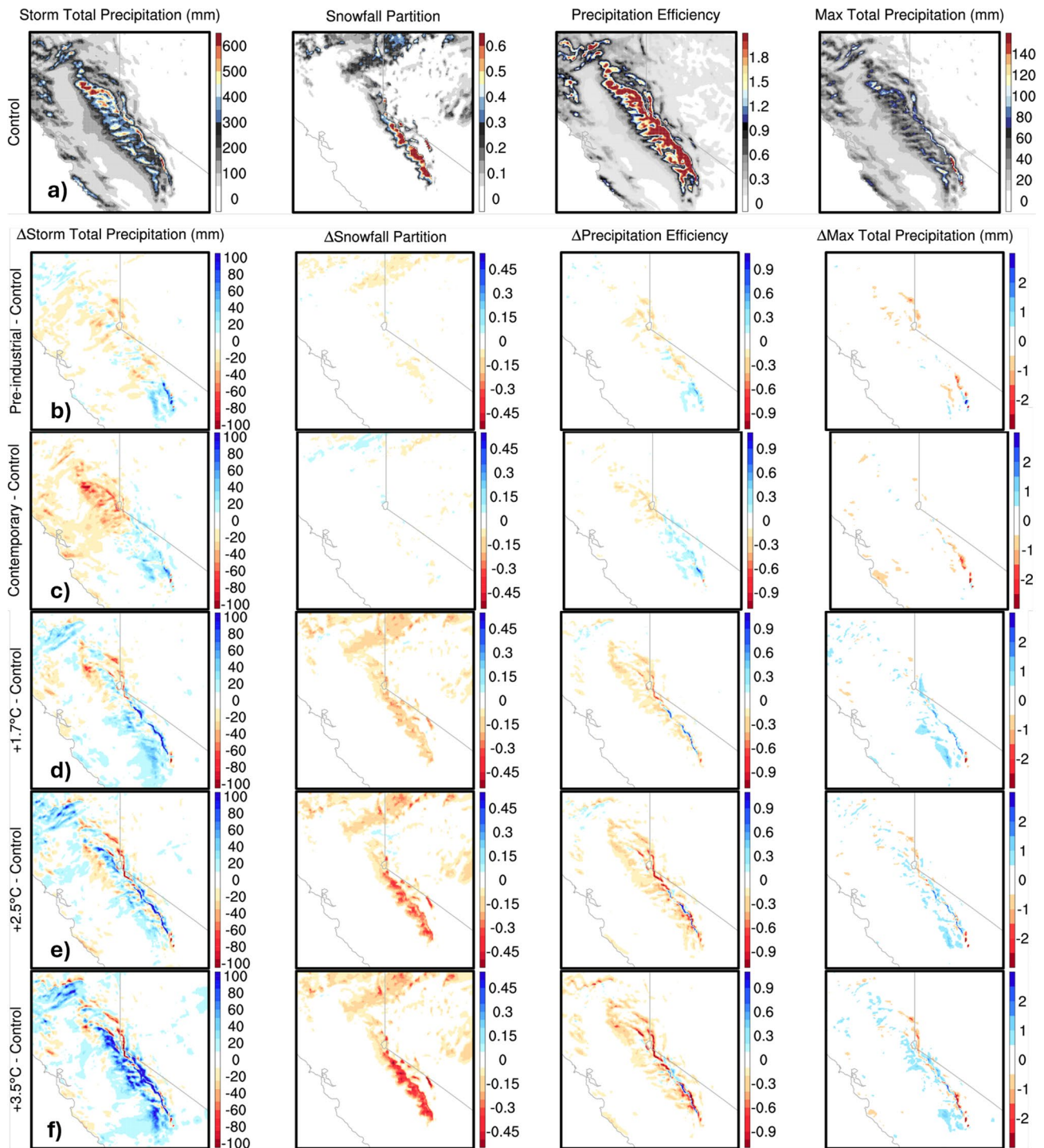
Fig. 2 RRM-E3SM (3.5 km) forecast average estimates of the difference in landfalling AR characteristics of the control simulation (**a**; top row) against the pre-industrial (**b**), contemporary (**c**), +1.7 °C (**d**), +2.5 °C (**e**) and +3.5 °C (**f**) experiments over the period of 31 December 1996 up to 4 January 1997. AR characteristics provided are the AR category (left column) and the storm duration maximum integrated vapor transport (IVT, second column), maximum integrated water vapor (IWV, third column), and maximum integrated total wind (right column). In each difference plot of the AR category, the gray area represents regions in the control simulation where categories 4–5 existed

Fig. 3 RRM-E3SM (3.5 km) forecast average estimates of the difference in precipitation characteristics from the control simulation (**a**; top row) against the pre-industrial (**b**), contemporary (**c**), +1.7 °C (**d**), +2.5 °C (**e**) and +3.5 °C (**f**) experiments over the period of 31 December 1996 up to 4 January 1997. Precipitation characteristics provided are the storm total precipitation (left column), snowfall partition of storm total precipitation (second column), precipitation efficiency (third column), and storm duration maximum total precipitation (right column)

these differences are based on six-forecast averages, they are arguably glimpses of a signal of warming rather than simply the noise of internal variability. At global warming levels representing both a contemporary (+0.4 °C) and near future (+1.7 °C) climate, less storm total precipitation is produced in northern portions of the California Sierra Nevada and more storm total precipitation occurs in the south. At warming levels above +2 °C, a more ubiquitous increase in storm total precipitation occurs across the California Sierra Nevada and northwestern portions of California. This is partly explained by slight increases in storm total moisture flux convergence, particularly on the windward side of the Sierra Nevada (Figs. S15 and S16). Further contributors are monotonic decreases in snowfall fraction and near-monotonic decreases in precipitation efficiency with warming. Unlike the rest of California, precipitation efficiency increases in southern portions of the leeward side of the Sierra Nevada in line with findings from previous studies (Siler and Roe 2014; Huang et al. 2020). Precipitation efficiency is defined as storm total precipitation divided by storm total integrated water vapor. This metric measures the efficiency of the terrain in extracting precipitation from the atmosphere, which warming has been shown to suppress in other mountainous regions (Eidhammer et al. 2018). Values of precipitation efficiency greater than one indicate grid cells where hydrometeors formed in one grid cell are then advected and fall out as precipitation in another (Fig. 3). Conversely, values less than one indicate a portion of atmospheric moisture that continues to be transported over the landscape. Across California, the precipitation efficiency is 0.33 in the control simulation and decreases to 0.29 at +3.5 °C. The precipitation efficiency in Nevada is more consistent between the control simulation (0.12) and at +3.5 °C (0.11).

Precipitation scaling with warming has been the focus of much research (Fowler et al. 2021a, b). It is often explained predominantly using thermodynamic concepts (e.g., the 7% increase per +1 °C in the saturation-specific humidity implied by the Clausius–Clapeyron relationship). Throughout the four-day event, California's mean storm total precipitation estimates across warming level simulations range between 106 and 117 mm, or a −3.2% (contemporary) to +7.2% (+3.5 °C) change from the control simulation. This is further confirmed when evaluated across the 52 precipitation gauge sites from the California Data Exchange Center (CDEC) used by the National Oceanic and Atmospheric Administration (NOAA) to produce the 1997 flood event storm summary (https://www.cnrfc.noaa.gov/storm_summaries/ol.php?storm=jan1997). Yet, across warming level experiments, the statistical distributions of storm total precipitation encompassing the mean, interquartile range, and extremes all overlap (Fig. 4). This overlap is maintained whether using the nearest grid cell to the precipitation gauge
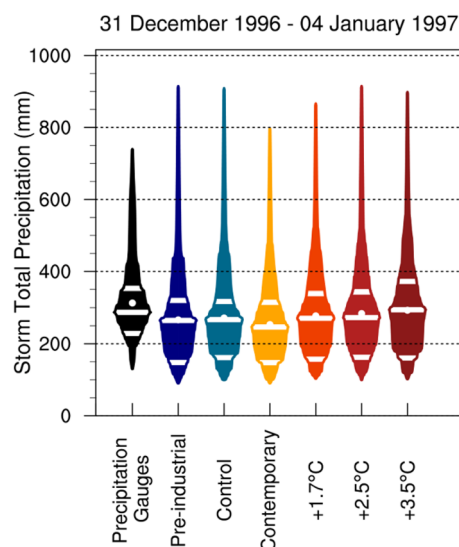

Fig. 4 Storm total precipitation (31 December 1996 up to 4 January 1997) evaluated at the 52 NOAA precipitation gauges within California. Violin plots represent the observed NOAA precipitation gauge precipitation measurements (black) and model estimates derived from the nearest grid cell to each gauge. Model estimates are color-coded by each warming level. The violin plots show the mean with a white dot, and white lines indicate the 25th, median, and 75th percentiles. The shape of each violin reflects the probability density function of the full distribution of the data

or using a 4 × 4 stencil average of the nearest grid cells to the precipitation gauge (Fig. S17).

Precipitation scaling in California-Nevada is dominated by stratiform precipitation from ARs and extra-tropical cyclones that interact with mountains, which may have different scaling properties compared to other storm types (e.g., convective) (Gershunov et al. 2019; Patricola et al. 2022). Storm total precipitation in the California Sierra Nevada scales at sub-Clausius–Clapeyron rates with warming (Fig. 5). Windward precipitation scales at smaller rates than leeward precipitation. This was predicted through theory by Siler and Roe (2014) via a warming-induced net downwind shift in mountain precipitation distributions. Mechanisms that drive this phenomenon include a warming-induced upward shift in the level of windward condensation, leading to increased leeward precipitation that is, in part, offset by faster hydrometeor fall speeds, and more adiabatic descent that induces leeside evaporation.

Unlike storm total precipitation, maximum hourly and sub-hourly precipitation rates on the windward side of the California Sierra Nevada scale at super-Clausius–Clapeyron rates (Fig. 5). Notably, 10-minute precipitation outputs are derived directly from EAM and the hourly outputs are gleaned from the 10-minute precipitation outputs by cumulative summing the 10-minute outputs over each hour. Leeside hourly and subhourly precipitation also scales consistently
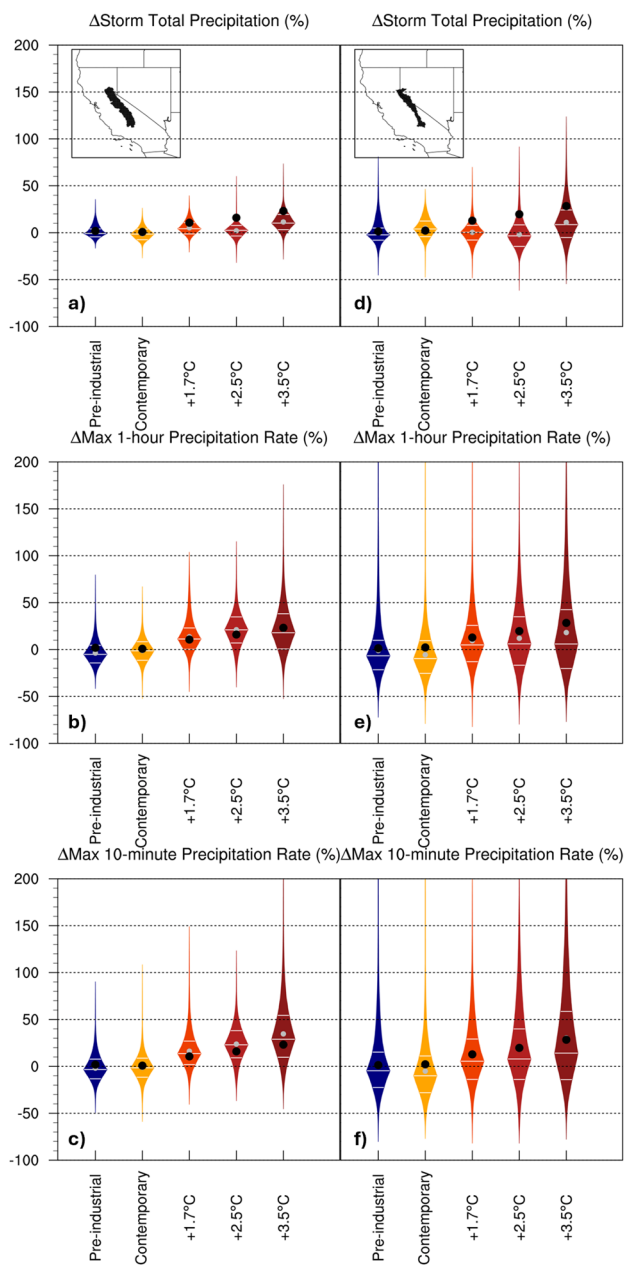
Fig. 5 Precipitation scaling with warming for storm total precipitation (**a**, **d**), max 1-h precipitation (**b**, **e**) and max 10-min precipitation (**c**, **f**) between 31 December 1996 up to 4 January 1997. Violin plots represent all the grid cells within the windward (**a–c**) and leeward (**d–f**) of the California Sierra Nevada. Windward and leeward shape regions are shown in black in the map plots. Model estimates are color-coded by each warming level. The violin plots show the mean with a gray dot, and gray lines indicate the 25th, median, and 75th percentiles. The shape of each violin reflects the probability density function of the data. Black dots show the expected precipitation scaling with warming based on the Clausius–Clapeyron equation devised by Bolton (1980)

with Clausius–Clapeyron, yet the percent changes span a wider range of possibilities. The difference in warming-induced precipitation scaling between storm total versus hourly-to-subhourly maximum precipitation rates alludes to the potential for abrupt bursts of precipitation occurring more systematically with warming, particularly along windward slopes (Fig. 3). Vertical profiles of changes in temperature, specific humidity, and static stability from the control simulation highlight that warming induces a more stable atmosphere over the entire 1997 flood duration at all pressure levels, likely due to warming aloft (Fig. S18). At lower pressure levels, warming-induced increases in specific humidity mute atmospheric stability through increases in latent static energy over the Sierra Nevada (Fig. S19). Therefore, differences between storm total precipitation and hourly-to-subhourly precipitation rates can be partly explained through a net dynamically-induced suppression of orographic uplift, offset at smaller timescales by enhanced thermodynamical feedbacks associated with enhanced moisture availability and enhanced latent heat release. This differential scaling of wintertime precipitation to warming at storm total versus hourly-to-subhourly timescales was also identified for the European Alps using ~3 km grid spacing regional climate model simulations (Ban et al. 2020).

At higher warming levels, our experiments indicate the shortest duration precipitation (i.e., subhourly) will come as rain instead of snow (Fig. 3). From both a storm total precipitation and maximum subhourly precipitation rate perspective, the majority of windward grid cells that produce the largest precipitation totals or rates occur in either the rain-snow transition and/or snowfall-dominated regions of the Sierra Nevada (Figs. 6, S20, S21). These regions also drive some of the largest deviations in precipitation from the control simulation with warming. Ombadi et al. (2023) also found warming-induced amplifications of precipitation in the rain-snow transition region across northern hemisphere mountains and across a larger ensemble of Earth system model simulations.

3.3 Despite enhanced rainfall, warming generally reduces the runoff response via low snow and drier soils, save for the southern, windward Sierra Nevada

The transition of snowfall to rainfall has a direct effect on rainfall-induced runoff. It also has an indirect effect through the warming-dependent changes in the accumulation of snowpack before the 1997 flood event. Further, the warming-induced snowfall-to-rainfall transition influences the timing and magnitude of snowmelt during the flood event. This is relevant as snowmelt was an important component of why the observed 1997 flood event was so costly and damaging. Figures 7 and S22 show different
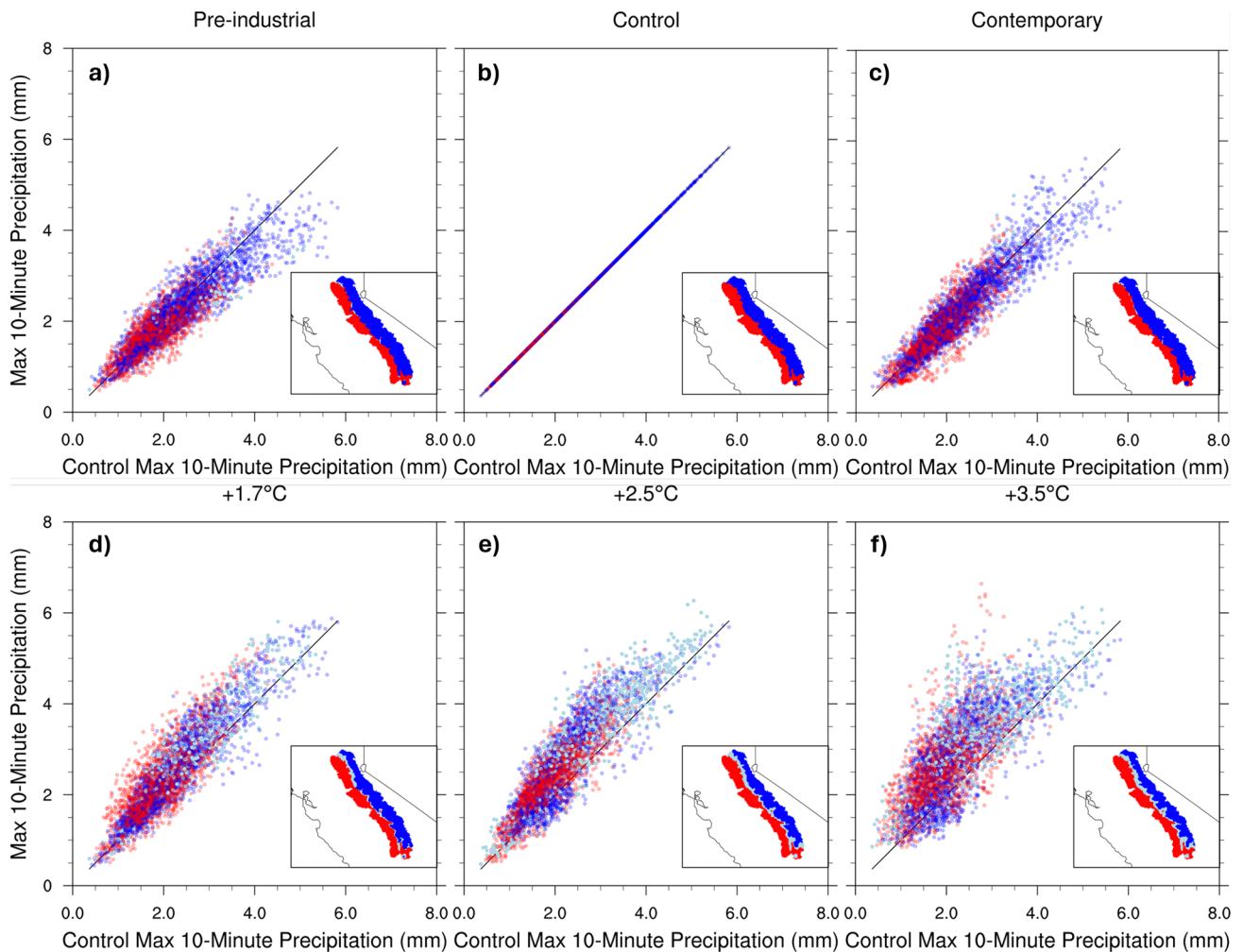
Fig. 6 Scatter plot comparisons of Sierra Nevada windward grid cells of max 10-min precipitation rates over the storm duration (31 December 1996 up to 4 January 1997) between the control (**b**) and pre-industrial (**a**), contemporary (**c**), +1.7 °C (**d**), +2.5 °C (**e**) and +3.5 °C (**f**) experiments. Subregions of the windward Sierra Nevada are color-coded to indicate rainfall, snowfall, and rain-snow transition with warming. Red dots indicate grid cells that purely experience rainfall over the storm duration. Blue dots indicate grid cells where snowfall occurs, at least, 2.54 mm over the storm duration. Light blue dots indicate grid cells where the control simulation has, at least, 2.54 mm of snowfall, yet the warming level simulation has purely rainfall. The black line indicates a 1:1 between the control simulation and each warming scenario

aspects of the snowpack characteristics on 31 December 1996 including snow water equivalent (SWE) and snow density. The pre-industrial and control simulations had nearly identical SWE volumes across California-Nevada (14.8 and 14.4 km^3, respectively) at the onset of the 1997 flood. Average snow densities (340–350 kg/m^3) were emblematic of a denser, late winter maritime snowpack (Sturm and Liston 2021) with average snow temperatures less than a quarter of a degree from freezing. As shown in Heggli et al. (2022) measured snow densities in the California Sierra Nevada an hour before historical RoS events ranged between 264 and 352 kg/m^3 (first and third quartiles, respectively) with a maximum measured value of 511 kg/m^3. In a more contemporary climate, average

SWE was reduced by 30% and average snow densities approached 370 kg/m^3. At warming levels ≥ 1.7 °C, SWE changes become quite pronounced in the windward Sierra Nevada (Fig. 7). Compared to the control simulation, Sierra Nevada-average SWE continues to be reduced by 43–76% and average snow densities increase by 50 kg/m^3 per +1 °C (400–500 kg/m^3), values typically achieved during the peak spring snowmelt season.

The combination of warmer, shallower, and denser snowpacks, particularly at warming levels greater than ≥ 1.7 °C, indicates that these snowpacks have lower cold content (closer to 0 MJ/m^2) and will produce meltwater with added energy. Half of the 31 December 1996 snowpack extent in the pre-industrial and control simulation
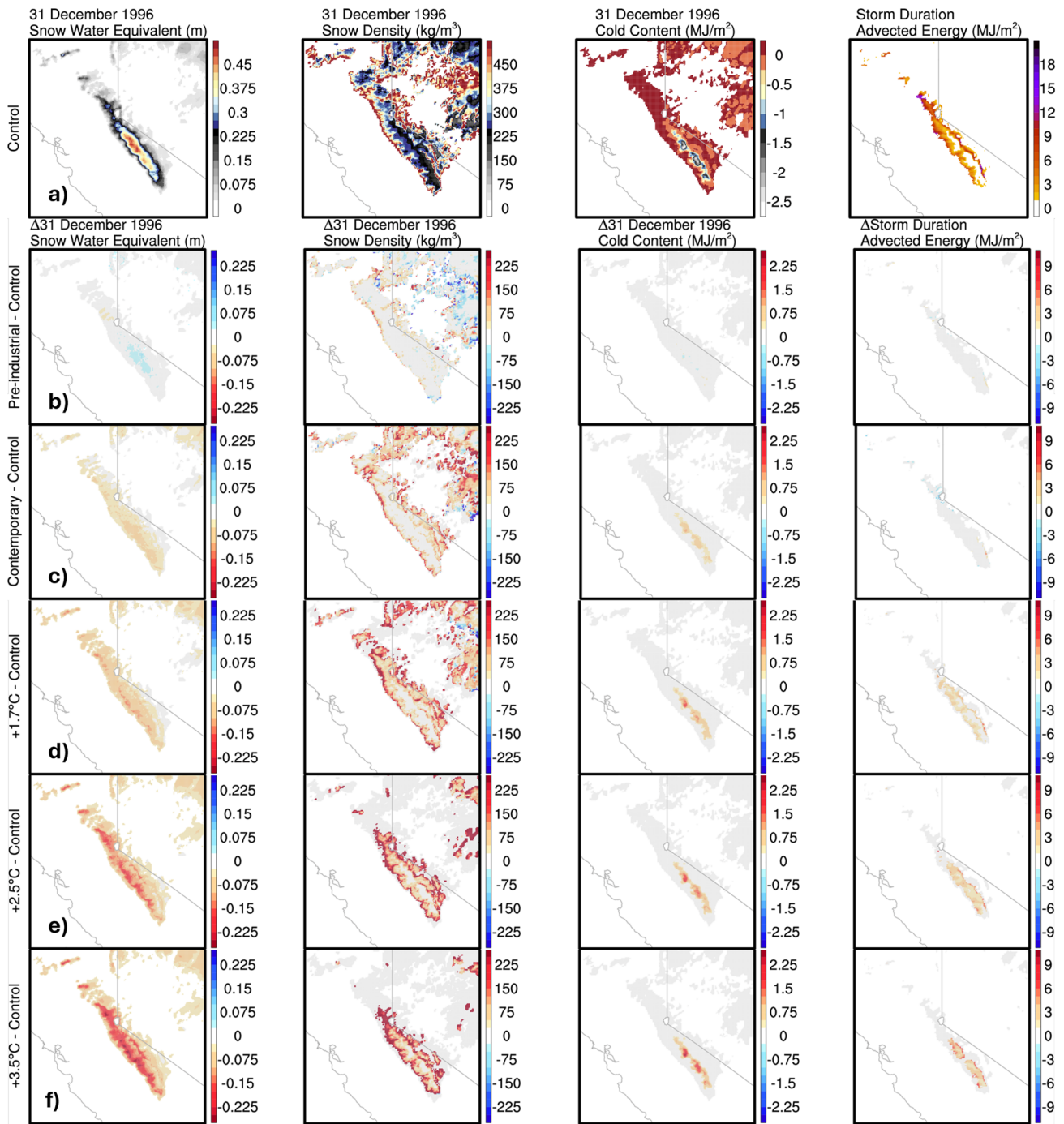
Fig. 7 RRM-E3SM (3.5 km) forecast average estimates of the difference in snowpack characteristics of the control simulation (**a**; top row) against the pre-industrial (**b**), contemporary (**c**), +1.7 °C (**d**), +2.5 °C (**e**) and +3.5 °C (**f**) experiments over the period of 31 December 1996 up to 4 January 1997. Snowpack characteristics pro-vided are the 31 December 1996 antecedent snow water equivalent (SWE; left column), antecedent snow density (second column), antecedent cold content (third column) and storm total advected energy (right column). In each of the difference plots the gray area represents the control simulation

had cold contents of 0 MJ/m^2 with the pre-industrial snowpack only 1.5% larger in area than the control (Fig. S22). In a contemporary climate, the 0 MJ/m^2 cold content area grows to 61% of the available snowpack, however, the snowpack area is also 26% smaller than the control. At warming levels of +2.5 and +3.5 °C, the 0 MJ/m^2 cold content area encompasses three-fourths (or more) of the

entire snowpack area, however, the snowpack area has also been reduced to one-third and one-fourth of the control simulation snowpack area, respectively. Importantly, even at higher elevations in the Sierra Nevada where the most robust (higher values) cold contents exist, minimum cold content values are reduced to 60% of the control simulation in a contemporary climate (-1.79 MJ/m^2) and systematically reduced by $\sim$15% per $+1$°C (-1.33 to -0.41 MJ/m^2).

Advected energy, the direct contribution of energy into the snowpack from precipitation (DeWalle and Rango 2008), becomes important when a snowpack's cold content approaches zero. We previously showed this is the case across all 1997 flood event simulations and during rain-dominated winter storm events, which ARs are often associated with (Hatchett et al. 2017; Shulgina et al. 2023). Positive advected energy values indicate an enhancement of energy to melt the snowpack whereas negative values indicate a diminishment of energy. Figures S22 and 7 show the advected energy provided during the event between 31 December 1996 to 04 January 1997. The highest storm duration advected energies occurred between $+1.7$ and $+2.5$ °C ($21.2-22.1$ MJ/m^2). This is likely due to the considerable snowpack available to melt on 31 December 1996 combined with a transition from snowfall to rainfall at mid-to-high elevations of the Sierra Nevada during the storm duration (Fig. 3). Figure S23 provides context for the percent contribution of advected energy to snowmelt energy relative to the total of sensible heat, latent heat, and advected energy. The mean contributed advected energy in the control RRM-E3SM simulation was 6.4%. Across all RRM-E3SM warming level experiments advected energy contribution ranged between 5.6% (pre-industrial) to 14% ($+3.5$ °C). This shows that although advected energy's contribution to the total potential snowmelt energy in any given grid cell more than doubles from pre-industrial to $+3.5$ °C, sensible and latent heat fluxes dominate the energy budget ($>$85% of the energy budget).

The net result of the storm duration interactions between precipitation phase changes, cold content, and advected energy is shown in Fig. 8 via plots of changes in SWE between 31 December 1996 to 04 January 1997. Storm duration changes in SWE are estimated at the closest grid cell to the 52 SNOTEL sites within the region evaluated throughout this study. Figure S24 shows the insensitivity of choosing the nearest grid cell estimates to those of a 4×4 stencil average of the surrounding grid cells nearest the SNOTEL sites. Unlike storm total precipitation discussed earlier, storm duration changes in SWE show a threshold-dependent sensitivity to warming. Pre-industrial through contemporary simulations all have similar estimates of both positive and negative changes in SWE over the storm duration. The center of mass of the distributions is below zero,
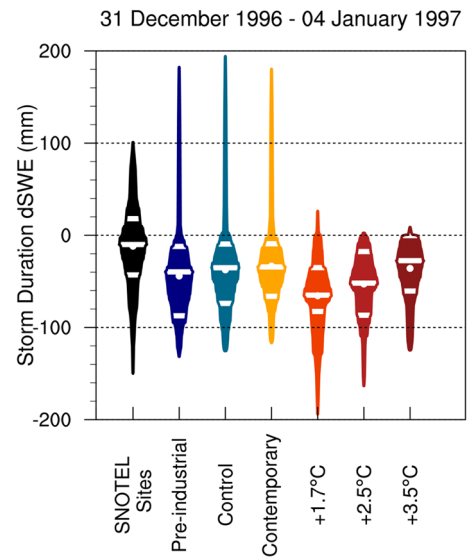

Fig. 8 Storm duration change in snow water equivalent, dSWE, (31 December 1996 up to 4 January 1997) evaluated at the 52 SNOTEL sites within California-Nevada. Violin plots represent the observed SNOTEL site dSWE during the 1997 flood event (black) and model estimate dSWE derived from the nearest grid cell to the 52 stations. Model estimates are color-coded by each warming level. The violin plots show the mean with a white dot, and white lines indicate the 25th, median, and 75th percentiles. The shape of each violin reflects the probability density function of the full distribution of the data

indicative of a primarily snowmelt-driven event. At warming levels $\geq$1.7 °C, snow accumulation is virtually non-existent during the 1997 flood event, with nearly the entire distribution below zero. The warming level that produces the most snowmelt is $+1.7$ °C because $+2.5$ and $+3.5$ °C have less antecedent snowpack.

The culmination of the interactions across the physical drivers of the 1997 flood event, and their warming level sensitivities, are shown through runoff. Figure 9 and S25 show the storm total runoff across warming levels. Spatial signatures of runoff changes with warming are coincident with regions where SWE is lost over the storm duration (Fig. 7) and in portions of the Sierra Nevada with higher soil moisture contents on 31 December 1996 (Fig. 9). Average storm total runoff changes with warming range between -17% in the $+3.5$ °C simulation to -26% in the $+2.5$ °C simulation. The lack of systematic signal with warming is likely due to the competing influences of increases and decreases in precipitation totals, soil moisture concentrations, and snowmelt. Runoff efficiency generally decreases across all warming levels, although important spatial signatures with warming are seen in both the northern versus southern and windward versus leeward side of the California Sierra Nevada. Windward runoff efficiency changes are latitude-dependent. The northern Sierra Nevada shows a systematic decrease with warming and the central to southern Sierra
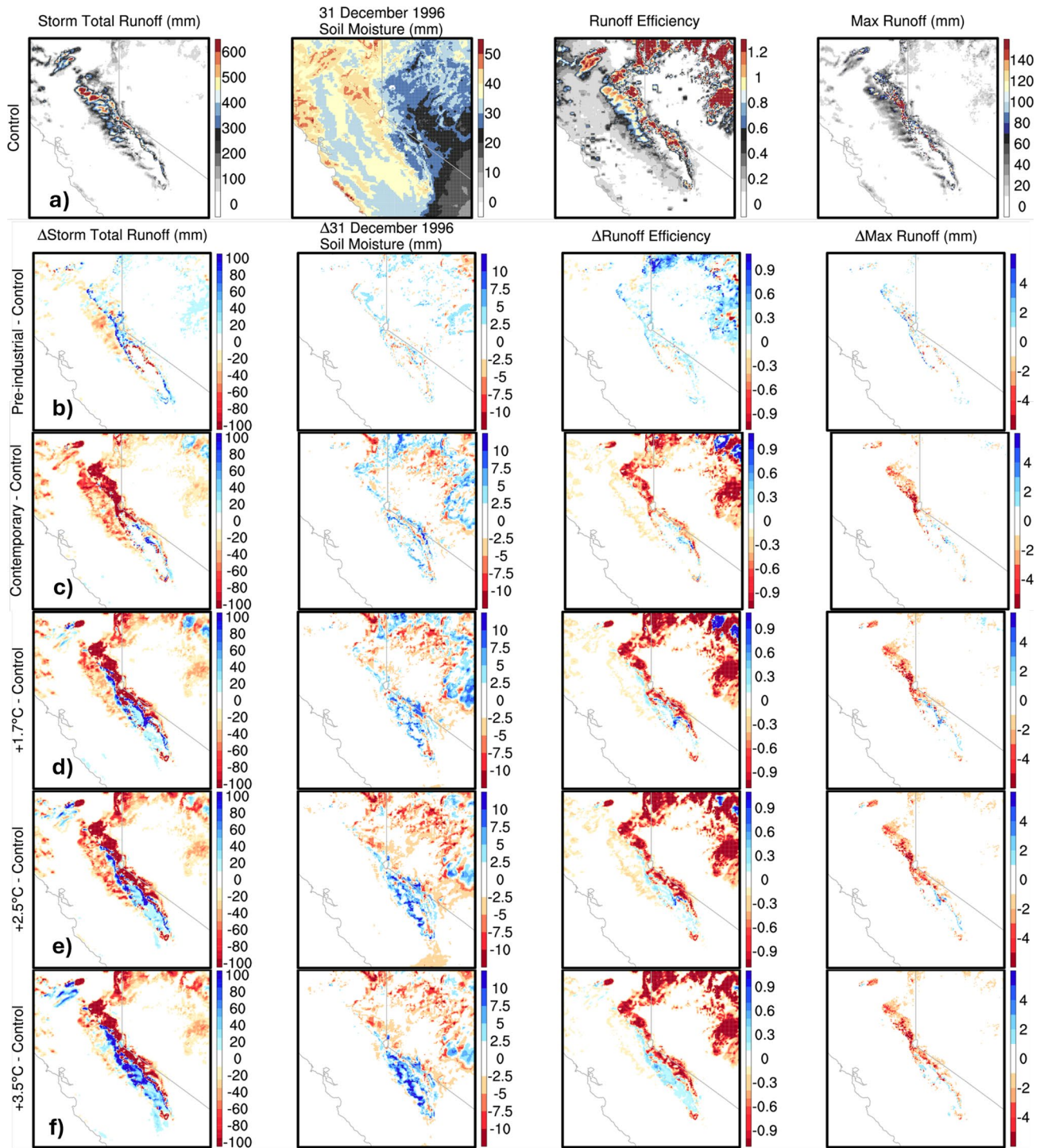
Fig. 9 RRM-E3SM (3.5km) forecast average estimates of the difference in runoff characteristics of the control simulation (**a**; top row) against the pre-industrial (**b**), contemporary (**c**), +1.7 °C (**d**), +2.5 °C (**e**) and +3.5 °C (**f**) experiments over the period of 31 December 1996 up to 4 January 1997. Runoff characteristics provided are the storm total runoff (left column), antecedent soil moisture on 31 December 1996 (second column), runoff efficiency (third column), and storm duration maximum runoff (right column)

Nevada indicates an increase. Leeward runoff efficiency systematically decreases with warming. Maximum runoff changes over the storm duration do have a more systematic

relationship to warming. Maximum 3-hourly runoff in the +1.7 to +3.5 °C simulations decrease between −24% (80 mm decrease) to −61% (200 mm decrease) compared to

the control simulation (330 mm). Notably, the pre-industrial simulation shows a 45% increase (or 150 mm increase) compared to the control simulation.

3.4 Summarizing the storm duration changes in the fluxes and stores of water during the 1997 flood across warming levels

To summarize all of the land-atmosphere interactions during the 1997 flood event we employ a Sankey diagram. Sankey diagrams explicitly show changes in the magnitude and direction of the key fluxes and stores of the hydrologic cycle and are often used to visually summarize water management (Curmi et al. 2013; Lehrman 2018). These diagrams demonstrate how competing factors interact with one another under warming to shape the storm duration water budgets. Each of the major natural water reservoirs are represented in km^3. These natural reservoirs represent the storm totals over the storm duration (31 December 1996 up to 04 January 1997) area averaged and multiplied by the shape region area. The fluxes of water between natural reservoirs are also shown as gray connectors.

At warming levels ≥1.7 °C, the hydrometeorological cycle during the 1997 flood becomes markedly different, particularly at +3.5 °C over California and Nevada (Fig. 10). All warming level experiments for California and Nevada are presented in Figs. S26 and S27. California-wide storm total precipitation increases (+1.5−3.5 km^3) even while precipitation efficiency (storm total precipitation/storm total integrated water vapor) decreases by 0.01 per warming level (0.29−0.31) compared to the control simulation (0.33). Offsetting the state-wide precipitation increases, storm total snowfall and antecedent snowpack reduces (−1.0 to −1.7 km^3 and −3.0 to −5.4 km^3, respectively). These effects of warming on storm total precipitation, snowfall, and antecedent snowpack are consistent in sign but different in magnitude across the Sierra Nevada and Nevada (Figs. S28, S29, and S27). The net effect is that storm total runoff decreases across California (−1.8 to −3.8 km^3) and Nevada (−1.3 to −2.4 km^3). However, when viewed from the perspective of the windward side of the Sierra Nevada (which feeds most of the reservoirs in the state), storm total runoff increases by +0.8 km^3 at +3.5 °C. This might be due to the spatiotemporal dependencies of runoff in the Sierra Nevada to factors such as the soil moisture wetting front shaped by snowline retreat and their interactions with underlying soil composition and permeability (Figs. 7 and 9). This could also be due to the increase in bursts of rainfall at hourly-to-subhourly timescales, particularly in the southern Sierra Nevada (Fig. 5).

A key question is how the hydrometeorological cycle of the 1997 flood event may have been impacted by 20th-century warming. Minor differences between the control and pre-industrial simulations are shown across the state of California (Fig. S26). All of the natural reservoirs, save for integrated water vapor, are within ±0.5 km^3 of one another (or ≤2% change). This is also true for the state of Nevada

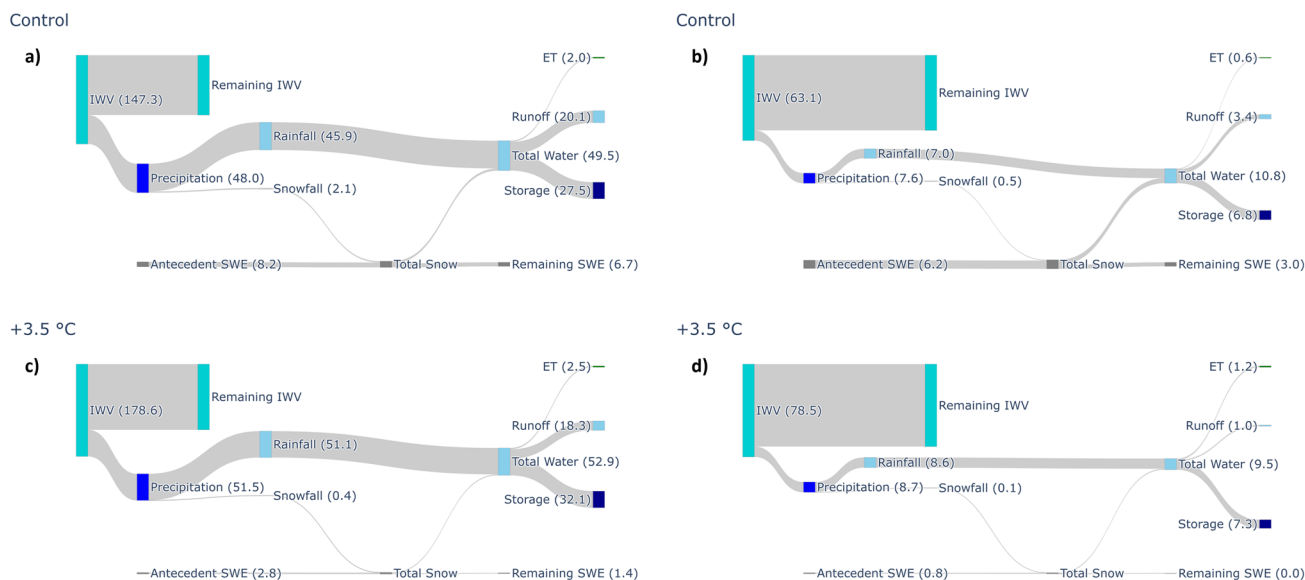**Fig. 10** Sankey diagrams of the natural reservoirs (colored bars; km^3) and flows of water (gray) within the control and +3.5°C experiments over the storm duration, 31 December 1996 up to 04 January 1997. Each natural reservoir is vertically sized by its volume (provided in parentheses). The natural reservoirs and flows are derived using only data within the borders of either California (**a**, **c**) or Nevada (**b**, **d**). Notably, reservoir sizes are scaled by region and care should be taken when visually comparing between regions

and the windward and leeward side of the Sierra Nevada (Figs. S27, S28, and S29, respectively). This indicates that the hydrometeorological variables that shaped hazards during the 1997 flood event had minimal sensitivity to warming over the 20th century. In a contemporary climate the precipitation response is more muted in California (-1.5 km^3) (Fig. S26). This also holds in Nevada and across the Sierra Nevada (Figs. S27, S28, and S29). Additionally, there is less antecedent snowpack to melt in California (-1.9 km^3) and Nevada (-2.1 km^3). A net reduction in statewide storm total runoff is found in California (-4 km^3) and Nevada (-1 km^3). The interacting influences of precipitation, snowmelt, and antecedent soil moisture on runoff show that if a 1997 flood-like event occurred in a more contemporary climate the runoff response could be more muted.

4 Discussion and conclusions

Compound extreme events, such as the 1997 flood event, driven by an AR and representative of a RoS event, provide unique hydrometeorological case studies to evaluate cutting-edge modeling frameworks such as RRM-E3SM. This is because the drivers of compound extreme events span all aspects of the mountainous hydrologic cycle and each part of the system could differ in its response to climatic change. These responses vary in magnitude and/or sign and can either amplify or diminish the hazards produced. For example, the Clausius–Clapeyron relationship is an amplifying feedback whereby atmospheric saturation specific humidity monotonically increases with warming, which increases the potential for enhanced precipitation to occur. Another example is the attenuation of equator-to-pole temperature gradients. This effect locally diminishes the Clausius–Clapeyron feedback through dynamically-induced alterations to the location, magnitude, and persistence of the jet stream. In turn, these alterations shift the landfall location, phase (translational) speed, and orographic uplift potential of storms. Furthermore, local-scale warming alters the rain-snow partitioning of the storms and diminishes the cold content of the snowpack. These cross-scale interactions can either amplify or diminish both the storm total runoff and maximum runoff rates based on the land surface's antecedent conditions (e.g., soil moisture) and precipitation characteristics (e.g., storm total precipitation vs subhourly precipitation rates).

The RRM-E3SM framework captures many of the aforementioned cross-scale interactions in a single-model approach. This allows for the identification of the fingerprints of climate change that most amplify and diminish flood drivers that shape decision-relevant, compound extreme events, such as the New Year's flood event of 1997.

With RRM-E3SM we identified the following ways the drivers of the 1997 flood event could respond to warming:

(1) 1997 flood hazards were not appreciably altered by current levels of climate change, yet begin to occur at warming levels $\geq +1.7°C$

(2) AR categories systematically increase with warming and hazardous categories cover larger areas of California

(3) Storm total precipitation increases with warming, but below expected rates estimated using the Clausius–Clapeyron relationship

(4) Hourly-to-subhourly precipitation rates increase with warming, particularly in the leeward side of the Sierra Nevada, exceeding Clausius–Clapeyron expectations at warming levels $\geq +1.7°C$

(5) Snowfall and SWE (both antecedent and storm duration changes) systematically decreases with warming, even at high elevations of the Sierra Nevada

(6) Antecedent soil moisture (31 Dec 1996) generally decreases with warming, especially in northern California, save for regions near the wetting front of snowline retreat

(7) Storm total runoff, maximum runoff rate, and runoff efficiency generally decrease with warming, except in the southern Sierra Nevada where antecedent snowpack can be maintained in a warmer world

Although our previous study (Rhoades et al. 2023) and this study robustly investigate different sources of uncertainty, namely those contributed by internal variability and emissions scenario (Lafferty and Sriver 2023), when projecting hydrometeorological cycle changes in a warmer future a caveat to our findings is that this is a single model, single RoS event investigation. This means that RRM-E3SM might project the flood hazard responses to warming in different ways than other modeling approaches (e.g., extreme precipitation scaling with warming; Thackeray et al. 2018; Sugiyama et al. 2010). Additionally, our modeling approach robustly represents the thermodynamic feedbacks of warming across the atmosphere, ocean, and land surface. Yet, we provide a limited representation of dynamical changes (e.g., latitudinal shift in storm tracks), other than those that arise over the duration of the 8-day forecasts in response to thermodynamical adjustments. The dynamical changes that occur over longer timescales, such as the latitudinal shift in the storm track, could play an important role in shaping the local hazards presented by a future 1997 flood-like event (Pfahl et al. 2017) by altering the landfall location of the AR event and its orthogonality to complex terrain. Similarly, the 1997 flood event may be a unique outlier compared to other RoS events (Katz et al. 2023). For example, Patricola et al. (2022) has shown that an AR's storm total precipitation

responds differently to warming when associated with a strong versus weak (or non-existent) extra-tropical cyclone. The AR that made landfall during the 1997 flood event is associated with a weak extra-tropical cyclone and therefore may have a muted precipitation response to warming compared to an AR associated with a strong extra-tropical cyclone. The interplay between ARs and extra-tropical cyclones highlights the need to explore a broader set of AR-induced flood events using RRM-E3SM, particularly from the perspective of storm total precipitation versus hourly-to-subhourly precipitation rate scaling with warming. Differences in AR precipitation characteristics with warming might also arise through changes in the latitude in which the AR makes landfall (Shields and Kiehl 2016), the landfall orthogonality of the AR storm track to complex terrain (Ricciotti and Cordeira 2022), and, importantly, the AR origin in the tropical or subtropical Pacific (Gonzales et al. 2019, 2022). The snowpack model in RRM-E3SM also presents sources of uncertainty in representing aspects of snowmelt during RoS events. This is because the model can not currently simulate preferential flow paths and has assumptions in how advected energy is incorporated into the snowpack. Both of these play an important role in snowmelt dynamics. Inclusion of preferential flow paths in the snowpack, which can contribute to runoff without snowmelt during rainfall, is limited in almost all snowpack models, however, the need to capture this process is established (Brandt et al. 2022) and progress is being made (Leroux et al. 2020). Additionally, we found that maximum snow densities reached in the control simulation near the snowline were too high ($\geq$600 kg/m^3; 7.6% of the total snow area) compared to observed RoS events (Heggli et al. 2022) and could also be addressed in future ELM development.

While low-snow and drier soil conditions are more widely accepted and expected in future RoS events (Siirila-Woodburn et al. 2021; Albano et al. 2022), short-duration bursts of rainfall are debated (Westra et al. 2014; Fowler et al. 2021a, b). Theory supports the notion that super Clausius–Clapeyron scaling of both hourly and subhourly precipitation with warming is possible (Westra et al. 2014). However, this is not always true for each region, season, and storm type. This is because the precipitation efficiency (or drying ratio) of a mountain is dependent on its geometry, its large-scale environment above and surrounding it, and the characteristics and lifecycle of the storm event (Smith et al. 2010; Eidhammer et al. 2018). For example, in the European Alps, modeling-based experiments (comparable in horizontal resolution to this study) found that summer and fall precipitation scaling rates with warming asymptote at the expected Clausius–Clapeyron rate (+7% per +1 °C) (Vergara-Temprado et al. 2021). This scaling relationship occurs at hourly to subhourly timescales and whether 700 hPa or two-meter surface air temperatures were used to normalize

the precipitation scaling. Yet, hourly precipitation rates in winter were shown at super Clausius–Clapeyron rates with warming (Ban et al. 2020). In California, observational evidence has shown that AR-precipitation scales at higher rates than non-AR precipitation and, in some instances, hourly maximum precipitation has exceeded Clausius–Clapeyron scaling (Najibi and Steinschneider 2023). Modeling studies have also shown that precipitation rates scale at super Clausius–Clapeyron rates with warming in California during other AR RoS events (Huang et al. 2020; Michaelis et al. 2022). Theory, observations, and the aforementioned modeling studies provide confidence that super Clausius–Clapeyron scaling of hourly to subhourly precipitation in the California Sierra Nevada could be expected during future AR RoS events.

This study highlights several take-home messages for water resource management and emergency managers on how RoS event behavior could change through the 21st century with continued warming. First, we identify that at +1.7 °C, maximum snowmelt occurs due to nonlinear reductions in snowpack at greater warming levels. This supports the "peak RoS" concept introduced by Heggli et al. (2022) and implies that at mid-century when Earth reaches a consistent +1.7 °C we could see a maxima in the potential for hazardous RoS events. However, if warming continues beyond +1.7 °C a diminishment in RoS events could occur as more persistent low-to-no snow conditions arise (Rhoades et al. 2022). Second, our findings indicate that future RoS events could include more intense short-duration bursts of rainfall in the rain-snow transition regions of the Sierra Nevada. More rainfall, that is also more intense, in these regions amplifies flood and landslide hazard to infrastructure and communities that reside within and downstream of mountains (Ombadi et al. 2023). Chen et al. (2023) found such bursts of rainfall might also occur more in the storm center, which has implications for flash floods and, in urbanized areas, stormwater impacts. Third, engineers often design infrastructure with scale factors that depend on estimates of Clausius–Clapeyron-based precipitation scaling (Martel et al. 2021). We show important differences in how precipitation scales with warming at storm total (4-day) versus subhourly (10-min) which has implications for hardening and managing infrastructure under future precipitation extremes. For example, a climate adaptation approach called forecast-informed reservoir operations (Steinschneider and Brown 2012; Delaney et al. 2020) would need to make sure that historical assumptions of inflow rates, flood pool space, and spillway rates are sufficient to handle the aforementioned changes in RoS event behavior. Fourth, as snowpack recedes to higher elevations, this shifts potential hazards from the northern portions of California-Nevada further south. This presents unique water management challenges, particularly

in California, where the northern portions of the state currently have more widespread automated monitoring networks, larger reservoirs and have invested more into infrastructure hardening. Furthermore, we found that lee-side precipitation scaling was enhanced relative to windward precipitation, supporting theory-based arguments presented by Siler and Roe (2014). This enhanced leeside spillover of precipitation, at enhanced rates, with warming has implications for water managers that exist in multi-agency, multi-state systems that already faced significant flooding in the observed 1997 flood (Kaplan et al. 2009). Last, we show that in a warmer world, the increases in AR strength do not always translate to elevated hazards. For example, in our study, category 4–5 conditions ("mostly to primarily hazardous to water resource management") are more systematically reached across California with warming. Yet, the antecedent and storm duration land surface conditions also change (e.g., drier soils and less snow), which offsets potential hazards over the storm duration. Importantly, short-duration bursts of rainfall would present new hazards (e.g., urban flooding) and may not always be mitigated by changes in land surface conditions. The afore-mentioned are important to consider as we identify and prioritize investments in projects to introduce resilience into infrastructure and update water management practices from the 20th to the 21st century. These investments will need to consider the important nonlinear tradeoffs in flood risk presented by future RoS events amidst changing atmospheric and land surface conditions.

Data Availability The RRM-E3SM data, analysis scripts and plotting scripts for this study can be found via a publicly accessible repository (Science Gateway) through the National Energy Research Scientific Computing Center - https://portal.nersc.gov/archive/home/a/arhoades/Shared/www/California_New_Years_Flood_1997.

Declarations

Conflict of interest The authors do not have any financial or non-financial conflict of interest to disclose.

Ethical approval This declaration does not apply to this work.

References

AghaKouchak A, Chiang F, Huning LS et al (2020) Climate extremes and compound hazards in a warming world. Ann Rev Earth Planet Sci 48(1):519–548. https://doi.org/10.1146/annurev-earth-071719-055228

Albano CM, McCarthy MI, Dettinger MD et al (2021) Techniques for constructing climate scenarios for stress test applications. Clim Change 164(3–4):33. https://doi.org/10.1007/s10584-021-02985-6

Albano CM, Abatzoglou JT, McEvoy DJ et al (2022) A multidataset assessment of climatic drivers and uncertainties of recent trends in evaporative demand across the continental United States. J Hydrometeorol 23(4):505–519. https://doi.org/10.1175/JHM-D-21-0163.1

Allan RP, Barlow M, Byrne MP et al (2020) Advances in understanding large-scale responses of the water cycle to climate change. Ann N Y Acad Sci 1472(1):49–75. https://doi.org/10.1111/nyas.14337

Ban N, Rajczak J, Schmidli J et al (2020) Analysis of alpine precipitation extremes using generalized extreme value theory in convection-resolving climate simulations. Clim Dyn 55(1–2):61–75. https://doi.org/10.1007/s00382-018-4339-4

Bindoff NL, Stott PA, AchutaRao KM et al (2013). Detection and attribution of climate change: From global to regional. https://doi.org/10.1017/CBO9781107415324.022

Bolton D (1980) The computation of equivalent potential temperature. Mon Weather Rev 108(7):1046–1053

Bowers C, Serafin KA, Tseng KC, et al (2023) Atmospheric river sequences as indicators of hydrologic hazard in historical reanalysis and gfdl spear future climate projections. Earth's Future 11(12):e2023EF003536. https://doi.org/10.1029/2023EF003536

Brandt WT, Haleakala K, Hatchett BJ et al (2022) A review of the hydrologic response mechanisms during mountain rain-on-snow.

Front Earth Sci 10:791760. https://doi.org/10.3389/feart.2022.791760

Brogli R, Heim C, Mensch J et al (2023) The pseudo-global-warming (pgw) approach: methodology, software package pgw4era5 v1.1, validation, and sensitivity analyses. Geosci Model Dev 16(3):907–926. https://doi.org/10.5194/gmd-16-907-2023

Chen X, Leung LR, Gao Y et al (2023) Sharpening of cold-season storms over the western United States. Nat Climate Change 13(2):167–173. https://doi.org/10.1038/s41558-022-01578-0

Copernicus Climate Change Service Climate Data Store (CDS) (2017) Copernicus Climate Change Service (C3S): ERA5: Fifth generation of ECMWF atmospheric reanalyses of the global climate. https://cds.climate.copernicus.eu/cdsapp#!/dataset/reanalysis-era5-pressure-levels?tab=overview

Corringham TW, McCarthy J, Shulgina T et al (2022) Climate change contributions to future atmospheric river flood damages in the western United States. Sci Reports 12(1):13747. https://doi.org/10.1038/s41598-022-15474-2

Curmi E, Fenner R, Richards K et al (2013) Visualising a stochastic model of Californian water resources using Sankey diagrams. Water Resour Manag 27:3035–3050. https://doi.org/10.1007/s11269-013-0331-2

Danabasoglu G, Lamarque JF, Bacmeister J, et al (2020) The community earth system model version 2 (cesm2). J Adv Model Earth Syst 12(2):e2019MS001916. https://doi.org/10.1029/2019MS001916

Davenport FV, Herrera-Estrada JE, Burke M, et al (2020) Flood size increases nonlinearly across the western united states in response to lower snow-precipitation ratios. Water Resour Res 56(1):e2019WR025571. https://doi.org/10.1029/2019WR025571

Delaney CJ, Hartman RK, Mendoza J, et al (2020) Forecast informed reservoir operations using ensemble streamflow predictions for a multipurpose reservoir in northern California. Water Resour Res 56(9):e2019WR026604. https://doi.org/10.1029/2019WR026604

DeWalle DR, Rango A (2008) Snowpack energy exchange: basic theory. Principles of snow hydrology. Cambridge University Press, Cambridge, pp 146–181. https://doi.org/10.1017/CBO9780511535673.007

Eidhammer T, Grubišić V, Rasmussen R et al (2018) Winter precipitation efficiency of mountain ranges in the Colorado Rockies under climate change. J Geophys Res Atmos 123(5):2573–2590. https://doi.org/10.1002/2017JD027995

Eyring V, Gillett N, Achuta Rao K et al (2021) Human influence on the climate system. Cambridge University Press, Cambridge, pp 423–552. https://doi.org/10.1017/9781009157896.005

Fowler HJ, Ali H, Allan RP et al (2021a) Towards advancing scientific knowledge of climate change impacts on short-duration rainfall extremes. Philos Trans R Soc A Math Phys Eng Sci 379(2195):20190542. https://doi.org/10.1098/rsta.2019.0542

Fowler HJ, Lenderink G, Prein AF et al (2021b) Anthropogenic intensification of short-duration rainfall extremes. Nat Rev Earth Environ 2(2):107–122. https://doi.org/10.1038/s43017-020-00128-6

Gates WL, Boyle JS, Covey C et al (1999) An overview of the results of the Atmospheric Model Intercomparison Project (AMIP I). Bull Am Meteorol Soc 80(1):29–56. https://doi.org/10.1175/1520-0477(1999)080<0029:AOOTRO>2.0.CO;2

Gershunov A, Shulgina T, Clemesha RE et al (2019) Precipitation regime change in Western North America: the role of Atmospheric Rivers. Sci Reports 9(1):1–11. https://doi.org/10.1038/s41598-019-46169-w

Gettelman A, Morrison H (2015) Advanced two-moment bulk microphysics for global models. Part i: Off-line tests and comparison with other schemes. J Clim 28(3):1268–1287. https://doi.org/10.1175/JCLI-D-14-00102.1

Golaz JC, Van Roekel LP, Zheng X, et al (2022) The DOE E3SM Model Version 2: Overview of the physical model and initial model evaluation. J Adv Model Earth Syst 14:e2022MS003156. https://doi.org/10.1029/2022MS003156

Gonzales KR, Swain DL, Nardi KM et al (2019) Recent warming of landfalling atmospheric rivers along the west coast of the United States. J Geophys Res Atmos 124(13):6810–6826. https://doi.org/10.1029/2018JD029860

Gonzales KR, Swain DL, Roop HA, et al (2022) Quantifying the relationship between atmospheric river origin conditions and landfall temperature. J Geophys Res Atmos 127(20):e2022JD037284. https://doi.org/10.1029/2022JD037284

Guan B, Waliser DE, Ralph FM et al (2016) Hydrometeorological characteristics of rain-on-snow events associated with atmospheric rivers. Geophys Res Lett 43(6):2964–2973. https://doi.org/10.1002/2016GL067978

Gutowski WJ, Ullrich PA, Hall A et al (2020) The ongoing need for high-resolution regional climate models: process understanding and stakeholder information. Bull Am Meteorol Soc 101(5):E664–E683. https://doi.org/10.1175/BAMS-D-19-0113.1

Haleakala K, Brandt WT, Hatchett BJ, et al (2022) Watershed memory amplified the Oroville rain-on-snow flood of February 2017. PNAS Nexus 2(1):pgac295. https://doi.org/10.1093/pnasnexus/pgac295

Harrop BE, Balaguru K, Golaz JC, et al (2023) Evaluating the water cycle over conus at the watershed scale for the energy exascale earth system model version 1 (e3smv1) across resolutions. J Adv Model Earth Syst 15(11):e2022MS003490. https://doi.org/10.1029/2022MS003490

Hatchett BJ, Daudert B, Garner CB et al (2017) Winter snow level rise in the northern Sierra Nevada from 2008 to 2017. Water 9(11):899. https://doi.org/10.3390/w9110899

Hatchett BJ, Koshkin AL, Guirguis K, et al (2023) Midwinter dry spells amplify post-fire snowpack decline. Geophys Res Lett 50(3):e2022GL101235. https://doi.org/10.1029/2022GL101235

Hegerl GC, Brönnimann S, Schurer A et al (2018) The early 20th century warming: anomalies, causes, and consequences. WIREs Climate Change 9(4):e522. https://doi.org/10.1002/wcc.522

Heggli A, Hatchett B, Schwartz A et al (2022) Toward snowpack runoff decision support. iScience 25(5):104240. https://doi.org/10.1016/j.isci.2022.104240

Hock R, Rasul G, Adler C, et al (2019) High mountain areas. In: IPCC Special Report on the Ocean and Cryosphere in a Changing Climate. https://www.ipcc.ch/srocc/chapter/chapter-2/

Huang X, Swain DL, Hall AD (2020) Future precipitation increase from very high resolution ensemble downscaling of extreme atmospheric river storms in California. Sci Adv 6(29):eaba1323. https://doi.org/10.1126/sciadv.aba1323

Hughes M, Neiman PJ, Sukovich E, et al (2012) Representation of the Sierra Barrier Jet in 11 years of a high-resolution dynamical reanalysis downscaling compared with long-term wind profiler observations. J Geophys Res Atmos 117(D18). https://doi.org/10.1029/2012JD017869

Immerzeel WW, Lutz AF, Andrade M et al (2020) Importance and vulnerability of the world's water towers. Nature 577(7790):364–369. https://doi.org/10.1038/s41586-019-1822-y

Jackson WL, Smillie GM, Martin MW (1997) Analysis of the hydrologic, hydraulic, and geomorphic attributes of the yosemite valley flood: January 1–3, 1997. Technical Report NPS/NRWRD/NRTR-97/129, pp 1–41. http://npshistory.com/publications/yose/nrtr-97-129.pdf

Kaplan ML, Adaniya CS, Marzette PJ, et al (2009) The role of upstream midtropospheric circulations in the Sierra Nevada enabling leeside (spillover) precipitation. Part ii: A secondary atmospheric river accompanying a midlevel jet. J Hydrometeorol 10(6):1327–1354. https://doi.org/10.1175/2009JHM1106.1

Kattlemann R (1997) Flooding from rain-on-snow in the Sierra Nevada. In: Destructive Water: Water-Caused Natural Disasters, Their Abatement and Control, Anaheim, California, p 412, https://books.google.com/books?hl=en &lr= &id=8nbLGQw5fckC &oi=fnd &pg=PA59 &dq=Kattlemann,+R.+(1997).+Flooding+from+rain-on-snow+events+in+the+Sierra+Nevada. &ots= Niz1IdG8Lg &sig=l1D6YcmTdNn5WlZJDJqjK6ZuUVE#v= onepage &q=Kattlemann%2C R. (1997). Flooding from rai

Katz L, Lewis G, Krogh S et al (2023) Antecedent snowpack cold content alters the hydrologic response to extreme rain-on-snow events. J Hydrometeorol 24(10):1825–1846. https://doi.org/10.1175/JHM-D-22-0090.1

Kay JE, Deser C, Phillips A et al (2015) The community earth system model (cesm) large ensemble project: a community resource for studying climate change in the presence of internal climate variability. Bull Am Meteorol Soc 96(8):1333–1349. https://doi.org/10.1175/BAMS-D-13-00255.1

Kumar S, Newman M, Lawrence DM et al (2020) The glace-hydrology experiment: effects of land-atmosphere coupling on soil moisture variability and predictability. J Climate 33(15):6511–6529. https://doi.org/10.1175/JCLI-D-19-0598.1

Lafferty DC, Sriver RL (2023) Downscaling and bias-correction contribute considerable uncertainty to local climate projections in CMIP6. NPJ Climate Atmos Sci 6(1):158. https://doi.org/10.1038/s41612-023-00486-0

Larson VE (2022) Clubb-silhs: A parameterization of subgrid variability in the atmosphere. https://doi.org/10.48550/arXiv.1711.03675, arXiv:1711.03675 [physics.ao-ph]

Lawrence DM, Fisher RA, Koven CD et al (2019) The community land model version 5: Description of new features, benchmarking, and impact of forcing uncertainty. J Adv Model Earth Syst 11(12):4245–4287. https://doi.org/10.1029/2018MS001583

Lehner F, Coats S (2021) Does regional hydroclimate change scale linearly with global warming? Geophys Res Lett 48(23):e2021GL095127. https://doi.org/10.1029/2021GL095127

Lehrman B (2018) Visualizing water infrastructure with Sankey maps: a case study of mapping the Los Angeles aqueduct, California. J Maps 14(1):52–64. https://doi.org/10.1080/17445647.2018.1473815

Leroux NR, Marsh CB, Pomeroy JW (2020) Simulation of preferential flow in snow with a 2-d non-equilibrium Richards model and evaluation against laboratory data. Water Resour Res 56(9):e2020WR027466. https://doi.org/10.1029/2020WR027466

López-Moreno JI, Pomeroy J, Morán-Tejeda E et al (2021) Changes in the frequency of global high mountain rain-on-snow events due to climate warming. Environ Res Lett 16(9):094021. https://doi.org/10.1088/1748-9326/ac0dde

Lott N, Sittel MC, Ross D (1997) The winter of '96-'97 : west coast flooding. National Climatic Data Center technical report; 97-01 pp 1–22. https://repository.library.noaa.gov/view/noaa/13812

Luce CH, Abatzoglou JT, Holden ZA (2013) The missing mountain water: slower westerlies decrease orographic enhancement in the Pacific Northwest USA. Science 342(6164):1360–1364. https://doi.org/10.1126/science.1242335

Martel JL, Brissette FP, Lucas-Picher P et al (2021) Climate change and rainfall intensity-duration-frequency curves: overview of science and guidelines for adaptation. J Hydrol Eng 26(10):03121001. https://doi.org/10.1061/(ASCE)HE.1943-5584.0002122

McCabe GJ, Clark MP, Hay LE (2007) Rain-on-snow events in the Western United States. Bull Am Meteorol Soc 88(3):319–328. https://doi.org/10.1175/BAMS-88-3-319

McGurk BJ, Marsh P (1995) Flow-finger continuity in serial thick-sections in a melting Sierran snowpack. Biogeochemistry of Seasonally Snow-Covered Catchments (Proceedings of a Boulder Symposium, July 1995) 1(228). http://www.researchgate.net/publication/246204567

Michaelis AC, Gershunov A, Weyant A, et al (2022) Atmospheric river precipitation enhanced by climate change: A case study of the storm that contributed to California's Oroville dam crisis. Earth's Future 10(3):e2021EF002537. https://doi.org/10.1029/2021EF002537

Mlawer EJ, Taubman SJ, Brown PD et al (1997) Radiative transfer for inhomogeneous atmospheres: Rrtm, a validated correlated-k model for the longwave. J Geophys Res Atmos 102(D14):16663–16682. https://doi.org/10.1029/97JD00237

Musselman KN, Lehner F, Ikeda K et al (2018) Projected increases and shifts in rain-on-snow flood risk over western North America. Nat Climate Change 8(9):808–812. https://doi.org/10.1038/s41558-018-0236-4

Najibi N, Steinschneider S (2023) Extreme precipitation-temperature scaling in California: the role of atmospheric rivers. Geophys Res Lett 50(14):e2023GL104606. https://doi.org/10.1029/2023GL104606

Neiman PJ, Sukovich EM, Ralph FM et al (2010) A seven-year wind profiler-based climatology of the windward barrier jet along California's Northern Sierra Nevada. Mon Weather Rev 138(4):1206–1233. https://doi.org/10.1175/2009MWR3170.1

Neiman PJ, Hughes M, Moore BJ et al (2013) Sierra barrier jets, atmospheric rivers, and precipitation characteristics in northern California: a composite perspective based on a network of wind profilers. Mon Weather Rev 141(12):4211–4233. https://doi.org/10.1175/MWR-D-13-00112.1

Ombadi M, Risser MD, Rhoades AM et al (2023) A warming-induced reduction in snow fraction amplifies rainfall extremes. Nature 619:305–310. https://doi.org/10.1038/s41586-023-06092-7

O'Brien TA, Wehner MF, Payne AE, et al (2022) Increases in future ar count and size: Overview of the artmip tier 2 cmip5/6 experiment. J Geophys Res Atmos 127(6):e2021JD036013. https://doi.org/10.1029/2021JD036013

Pall P, Patricola CM, Wehner MF et al (2017) Diagnosing conditional anthropogenic contributions to heavy Colorado rainfall in September 2013. Weather Climate Extremes 17:1–6. https://doi.org/10.1016/j.wace.2017.03.004

Patricola CM, Wehner MF, Bercos-Hickey E et al (2022) Future changes in extreme precipitation over the San Francisco bay area: Dependence on atmospheric river and extratropical cyclone events. Weather Climate Extremes 36:100440. https://doi.org/10.1016/j.wace.2022.100440

Payne AE, Demory ME, Leung LR et al (2020) Responses and impacts of atmospheric rivers to climate change. Nat Rev Earth Environ 1:143–157. https://doi.org/10.1038/s43017-020-0030-5

Pepin N, Bradley RS, Diaz H et al (2015) Elevation-dependent warming in mountain regions of the world. Nat Climate Change 5(5):424–430. https://doi.org/10.1038/nclimate2563

Pepin NC, Arnone E, Gobiet A, et al (2022) Climate changes and their elevational patterns in the mountains of the world. Rev Geophys 60(1):e2020RG000730. https://doi.org/10.1029/2020RG000730

Pettett A, Zarzycki CM (2023) The 1996 mid-Atlantic winter flood: exploring climate risk through a storyline approach. J Hydrometeorol. https://doi.org/10.1175/JHM-D-22-0146.1

Pfahl S, O'Gorman PA, Fischer EM (2017) Understanding the regional pattern of projected future changes in extreme precipitation. Nat Climate Change 7(6):423–427. https://doi.org/10.1038/nclimate3287

Ralph FM, Rutz JJ, Cordeira JM et al (2019) A scale to characterize the strength and impacts of atmospheric rivers. Bull Am Meteorol Soc 100(2):269–289. https://doi.org/10.1175/BAMS-D-18-0023.1

Reynolds RW, Smith TM, Liu C et al (2007) Daily high-resolution-blended analyses for sea surface temperature. J Climate 20(22):5473–5496. https://doi.org/10.1175/2007JCLI1824.1

Rhoades AM, Ullrich PA, Zarzycki CM et al (2018) Sensitivity of mountain hydroclimate simulations in variable-resolution cesm to microphysics and horizontal resolution. J Adv Model Earth Syst 10(6):1357–1380. https://doi.org/10.1029/2018MS001326

Rhoades AM, Jones AD, O'Brien TA, et al (2020a) Influences of North Pacific Ocean Domain Extent on the Western U.S. Winter hydroclimatology in variable-resolution CESM. J Geophys Res Atmos 125(14):e2019JD031977. https://doi.org/10.1029/2019JD031977

Rhoades AM, Jones AD, Srivastava A, et al (2020b) The shifting scales of Western U.S. landfalling atmospheric rivers under climate change. Geophys Res Lett 47(17):e2020GL089096. https://doi.org/10.1029/2020GL089096

Rhoades AM, Risser MD, Stone DA et al (2021) Implications of warming on western United States landfalling atmospheric rivers and their flood damages. Weather Climate Extremes 32:100326. https://doi.org/10.1016/j.wace.2021.100326

Rhoades AM, Hatchett BJ, Risser MD et al (2022) Asymmetric emergence of low-to-no snow in the midlatitudes of the American cordillera. Nat Climate Change 12(12):1151–1159. https://doi.org/10.1038/s41558-022-01518-y

Rhoades AM, Zarzycki CM, Inda-Diaz HA, et al (2023) Recreating the California new year's flood event of 1997 in a regionally refined earth system model. J Adv Model Earth Syst 15(10):e2023MS003793. https://doi.org/10.1029/2023MS003793

Ricciotti JA, Cordeira JM (2022) Summarizing relationships among landfalling atmospheric rivers, integrated water vapor transport, and California watershed precipitation 1982–2019. J Hydrometeorol 23(9):1439–1454. https://doi.org/10.1175/JHM-D-21-0119.1

Richter JH, Sassi F, Garcia RR (2010) Toward a physically based gravity wave source parameterization in a general circulation model. J Atmos Sci 67(1):136–156. https://doi.org/10.1175/2009JAS3112.1

Santer BD, Painter JF, Mears CA et al (2013) Identifying human influences on atmospheric temperature. Proc Natl Acad Sci USA 110(1):26–33. https://doi.org/10.1073/pnas.1210514109

Schär C, Frei C, Lüthi D et al (1996) Surrogate climate-change scenarios for regional climate models. Geophys Res Lett 23(6):669–672. https://doi.org/10.1029/96GL00265

Shepherd TG (2019) Storyline approach to the construction of regional climate change information. Proc R Soc A Math Phys Eng Sci 475(2225):20190013. https://doi.org/10.1098/rspa.2019.0013

Shepherd TG, Boyd E, Calel RA et al (2018) Storylines: an alternative approach to representing uncertainty in physical aspects of climate change. Clim Change 151:555–571. https://doi.org/10.1007/s10584-018-2317-9

Shields CA, Kiehl JT (2016) Atmospheric river landfall-latitude changes in future climate simulations. Geophys Res Lett 43(16):8775–8782. https://doi.org/10.1002/2016GL070470

Shields CA, Rutz JJ, Leung LY et al (2018) Atmospheric river tracking method intercomparison project (artmip): project goals and experimental design. Geosci Model Dev 11(6):2455–2474. https://doi.org/10.5194/gmd-11-2455-2018

Shulgina T, Gershunov A, Hatchett BJ et al (2023) Observed and projected changes in snow accumulation and snowline in California's snowy mountains. Climate Dyn 61(9):4809–4824. https://doi.org/10.1007/s00382-023-06776-w

Siirila-Woodburn E, Rhoades A, Hatchett B et al (2021) Evidence of a low-to-no snow future and its impacts on water resources in the western United States. Nat Rev Earth Environ 2:800–819. https://doi.org/10.1038/s43017-021-00219-y

Siler N, Roe G (2014) How will orographic precipitation respond to surface warming? an idealized thermodynamic perspective. Geophys Res Lett 41(7):2606–2613. https://doi.org/10.1002/2013GL059095

Smith BL, Yuter SE, Neiman PJ et al (2010) Water vapor fluxes and orographic precipitation over Northern California associated with a landfalling atmospheric river. Mon Weather Rev 138(1):74–100. https://doi.org/10.1175/2009MWR2939.1

Steinschneider S, Brown C (2012) Dynamic reservoir management with real-option risk hedging as a robust adaptation to nonstationary climate. Water Resour Res 48(5). https://doi.org/10.1029/2011WR011540

Stevenson S, Coats S, Touma D et al (2022) Twenty-first century hydroclimate: a continually changing baseline, with more frequent extremes. Proc Natl Acad Sci USA 119(12):e2108124119. https://doi.org/10.1073/pnas.2108124119

Sturm M, Liston GE (2021) Revisiting the global seasonal snow classification: an updated dataset for earth system applications. J Hydrometeorol 22(11):2917–2938. https://doi.org/10.1175/JHM-D-21-0070.1

Sugiyama M, Shiogama H, Emori S (2010) Precipitation extreme changes exceeding moisture content increases in miroc and ipcc climate models. Proc Natl Acad Sci USA 107(2):571–575. https://doi.org/10.1073/pnas.0903186107

Tang Q, Golaz JC, Van Roekel LP et al (2022) The fully coupled regionally refined model of E3SM Version 2: overview of the atmosphere, land, and river. Geosci Model Dev Discuss 2022:1–64. https://doi.org/10.5194/gmd-2022-262

Tarouilly E, Li D, Lettenmaier DP (2021) Western U.S. superfloods in the recent instrumental record. Water Resour Res 57(9):e2020WR029287. https://doi.org/10.1029/2020WR029287

Taylor MA, Guba O, Steyer A, et al (2020) An energy consistent discretization of the nonhydrostatic equations in primitive variables. J Adv Model Earth Syst 12(1):e2019MS001783. https://doi.org/10.1029/2019MS001783

Thackeray CW, DeAngelis AM, Hall A et al (2018) On the connection between global hydrologic sensitivity and regional wet extremes. Geophys Res Lett 45(20):11343–11351. https://doi.org/10.1029/2018GL079698

Trenberth KE (1995) Truncation and use of model-coordinate data. Tellus A 47(3):287–303. https://doi.org/10.1034/j.1600-0870.1995.t01-1-00001.x

Ullrich PA, Zarzycki CM (2017) TempestExtremes: a framework for scale-insensitive pointwise feature tracking on unstructured grids. Geosci Model Dev 10(3):1069–1090. https://doi.org/10.5194/gmd-10-1069-2017

Ullrich PA, Xu Z, Rhoades A et al (2018) California's drought of the future: a midcentury recreation of the exceptional conditions of 2012–2017. Earth's Future 6(11):1568–1587. https://doi.org/10.1029/2018EF001007

Ullrich PA, Zarzycki CM, McClenny EE et al (2021) Tempestextremes v2.1: a community framework for feature detection, tracking, and analysis in large datasets. Geosci Model Dev 14(8):5023–5048. https://doi.org/10.5194/gmd-14-5023-2021

Vergara-Temprado J, Ban N, Schär C (2021) Extreme sub-hourly precipitation intensities scale close to the Clausius-Clapeyron rate over Europe. Geophys Res Lett 48(3):e2020GL089506. https://doi.org/10.1029/2020GL089506

Wang H, Easter RC, Zhang R, et al (2020) Aerosols in the e3sm version 1: New developments and their impacts on radiative forcing. J Adv Model Earth Syst 12(1):e2019MS001851. https://doi.org/10.1029/2019MS001851

Westra S, Fowler HJ, Evans JP et al (2014) Future changes to the intensity and frequency of short-duration extreme rainfall. Rev Geophys 52(3):522–555. https://doi.org/10.1002/2014RG000464

Zarzycki CM, Jablonowski C (2015) Experimental tropical cyclone forecasts using a variable-resolution global model. Mon Weather Rev 143(10):4012–4037. https://doi.org/10.1175/MWR-D-15-0159.1

Zhang G, McFarlane NA (1995) Sensitivity of climate simulations to the parameterization of cumulus convection in the Canadian climate centre general circulation model. Atmosphere-Ocean 33(3):407–446. https://doi.org/10.1080/07055900.1995.9649539

Zscheischler J, Westra S, Van Den Hurk BJ et al (2018) Future climate risk from compound events. Nat Climate Change 8(6):469–477. https://doi.org/10.1038/s41558-018-0156-3